Non-linear Ultrasound Imaging

Du, Yigang

Publication date:
2011

Document Version
Publisher's PDF, also known as Version of record

Technical University
of Denmark

Non-linear Ultrasound Imaging

Yigang Du

May 2011

DTU Electrical Engineering
Department of Electrical Engineering

Center for Fast Ultrasound Imaging
Department of Electrical Engineering
Technical University of Denmark
DK-2800 Kgs. Lyngby, Denmark
&
BK Medical Aps
DK-2730 Herlev, Denmark

Submitted in partial fulfillment of the requirements for the degree of Doctor of Philosophy at the Technical University of Denmark.

Preface

In December 2007, I started to work at the Center for Fast Ultrasound Imaging (CFU) as a research assistant. This was the first time I was introduced to medical ultrasound imaging systems. Subsequently, I commenced my industrial PhD, specifically working with non-linear ultrasound imaging. Since modeling for non-linear ultrasound is highly related to the derivation of mathematical formulae, I believe this to be a mathematics challenge. Being an industrial PhD has taught me a lot about the project - also the commercial aspects when taking a business course at the Copenhagen Business School. Through participating in international ultrasound symposiums, I have had opportunities to communicate with people doing relevant science and sharing my experiences in ultrasound with research groups from all over the world. During my PhD study period, I have been not just a student but also functioned as a teaching assistant. This has provided me with a good teaching experience and taught me how to communicate with students as a teacher.

The dissertation was made at the end of the PhD study and based on work carried out from June 1st, 2008 to May 31st 2011 at the CFU, Technical University of Denmark as well as BK Medical Aps. To ease your reading, the main thesis will present the theory and results. Some complicated equation derivations and supplemental figures have been placed in the Appendix.

I hope very much that you will enjoy reading the dissertation and find the information you gain useful.

Yigang Du
May, 2011

Acknowledgments

First and foremost, I would like to express my deepest appreciation to my principal supervisor Professor Jørgen Arendt Jensen, head of the Center for Fast Ultrasound Imaging (CFU), at the Technical University of Denmark (DTU), for giving me the opportunity to enter the complicated but very interesting and amazing non-linear world of medical ultrasound imaging. He has always provided me with valuable advice and kept me on the right track in my research.

I sincerely thank my company supervisor Henrik Jensen for the useful and efficient discussions and suggestions to my project.

Also, I would like to thank all my current and former colleagues for creating such a great academic working place, where ideas and concepts can be shared, numerous discussions and creative cooperations on ultrasound have taken place and have given me a lot of support and inspiration for my project.

Furthermore, I would like to thank Henrik Laursen for helping me with numerous IT problems, Elna Sørensen and Nina Kjærgaard for the administrative assistance and written texts correction.

Last but absolutely not least, I would like to thank my parents for their unlimited love and support from the other side of the earth - Beijing, my favorite place and city of birth.

The PhD project was supported by grant 08-032480 from the Danish Agency for Science, Technology and Innovation, and by BK Medical Aps, Denmark.

Abstract

The theory for modeling non-linear acoustic propagation is addressed in the dissertation. The solutions to both the linear and non-linear wave equations have been found by an angular spectrum approach (ASA), in which an analytical expression can be derived. This makes the calculation complete without iteration steps. The ASA is implemented in combination with Field II and extended to simulate the pulsed ultrasound fields. The simulated results from a linear array transducer are made by the ASA based on Field II, and by a released non-linear simulation program - Abersim, respectively. The calculation speed of the ASA is increased approximately by a factor of 140. For the second harmonic point spread function the error of the full width is 1.5% at -6 dB and 6.4% at -12 dB compared to Abersim. To further investigate the linear and non-linear ultrasound fields, hydrophone measurements are performed under water by two geometrical focused piston transducers. It can be seen that the time pulses measured from a 0.5 inch diameter transducer and linearly simulated using the ASA are fairly comparable. The root mean square (RMS) error for the second harmonic field simulated by the ASA is 10.3% relative to the measurement from a 1 inch diameter transducer.

A preliminary study for harmonic imaging using synthetic aperture sequential beamforming (SASB) has been demonstrated. A wire phantom underwater measurement is made by an experimental synthetic aperture real-time ultrasound scanner (SARUS) with a linear array transducer. The second harmonic imaging is obtained by a pulse inversion technique. The received data is beamformed by the SASB using a Beamformation Toolbox. In the measurements the lateral resolution at -6 dB is improved by 66% compared to the conventional imaging algorithm. There is also a 35% improvement for the lateral resolution at -6 dB compared with the sole harmonic imaging and a 46% improvement compared with merely using the SASB.

List of Figures

List of Tables

Contents

Nomenclature

c_0	speed of sound
P_i	medium instantaneous pressure
P_e	medium equilibrium pressure
ρ	medium instantaneous density
ρ_0	medium equilibrium density
γ	ratio of specific heats
k	wave number
k_x	transverse wave number along x direction
k_y	transverse wave number along y direction
$\vec{u}$	particle velocity of a fluid element
t	time
p	acoustic pressure
β	coefficient of nonlinearity
p_1	fundamental component of the acoustic pressure
p_2	second harmonic component of the acoustic pressure
p_n	the nth harmonic component of the acoustic pressure
$P_n(x, y, z)$	amplitude of the sound wave of the nth harmonic as a function of space
ω	fundamental angular frequency
$c.c.$	complex conjugate of the preceding term
$\hat{P}_0(k_x, k_y, z_0)$	2D (x-y) spatial Fourier transform of $P_0(x, y, z_0)$
$\hat{P}_1(k_x, k_y, z_1)$	2D (x-y) spatial Fourier transform of $P_1(x, y, z_1)$
$\hat{P}_2(k_x, k_y, z_1)$	2D (x-y) spatial Fourier transform of $P_2(x, y, z_1)$
$\hat{P}_3(k_x, k_y, z_1)$	2D (x-y) spatial Fourier transform of $P_3(x, y, z_1)$
s	condensation
$\mathcal{F}\{\cdot\}$	Fourier transform

Abbreviations

ASA	Angular Spectrum Approach
CT	Computed Tomography
DRF	Dynamic Receive Focus
DRFI	Dynamic Receive Focus Imaging
DRFHI	Dynamic Receive Focus Harmonic Imaging
FWHM	Full Width at Half Maximum
FWOTM	Full Width at One Tenth Maximum
GPIB	General Purpose Interface Bus
HI	Harmonic Imaging
MRI	Magnetic Resonance Imaging
OSM	Operator Splitting Method
PET	Positron Emission Tomography
PI	Pulse Inversion
RMS	Root Mean Square
SARUS	Synthetic Aperture Real-time Ultrasound Scanner
SASB	Synthetic Aperture Sequential Beamforming
SASBHI	Synthetic Aperture Sequential Beamforming Harmonic Imaging
SASBI	Synthetic Aperture Sequential Beamforming Imaging
SNR	Signal-to-Noise Ratio

CHAPTER

ONE

Introduction

Medical ultrasound imaging is a non-invasive diagnostic technique, where the ultrasound wave is emitted into the human body and the image is made by processing the reflected ultrasound signals. Currently, ultrasound imaging plays an important role in medical diagnosis due to its safety, little discomfort, inexpensiveness and speediness compared with other medical imaging techniques. There is no ionizing radiation from ultrasound rather than an X-ray or CT scan, and no known harm to the patient of the ultrasound scan has been reported. The ultrasound image can be displayed in real-time, which is much faster than MRI. Furthermore, the instrument for an ultrasound system is relatively portable and less expensive than other systems such as MRI, CT or PET scanners.

However in general the ultrasound image visibly has more speckles and less clarity than the CT or MRI. In terms of the mechanism of ultrasound scanning, a relatively larger wavelength will give rise to a comparatively less directional beam and weak focusing as well as higher sidelobe. This will cause the distortion of the image and reduce the image quality since some artifacts which are not from the scanning area are displayed. Reducing the wavelength also means increasing the center frequency of the transducer. This will decrease the SNR, since the attenuation of the medium is to some extent directly proportional to the sending frequency. Thus, there must be compromise, where the ultrasound imaging can be optimized and improved.

At present, the improvement on ultrasound imaging can be achieved by numerous methods through, for example, transmitting a long pulse wave to enhance the SNR such as chirp-coded imaging, synthetic aperture imaging to achieve dynamic focusing in both transmit and receive, two-dimensional array transducers to generate 3D ultrasound images, compounding imaging

to reduce the clutter and artifacts and non-linear imaging to enhance the resolution and contrast.

This project is focused on the non-linear ultrasound imaging, which is extensively used in the clinic due to its improved image quality [1,2]. The images are formed by emitting at the fundamental frequency and receiving at the second harmonic. The isolation of the second harmonic can be done by directly filtering the received signal at the second harmonic [2]. The drawback of this is the limitation on bandwidth, and, thus resolution.

The problem has been solved by using pulse inversion imaging [1,3,4], where two pulses are emitted with opposite signs. Adding the pulse will remove the linear component and preserve the second harmonic component. It has been observed that the contrast is significantly better. This is probably due to the lower sidelobes in non-linear fields resulting in a higher contrast. The improvement is so vast that non-linear imaging is preferred in most investigations [2]. Thus, there is considerable interest and clinical value in using non-linear imaging.

Currently there is a limited understanding of the inner workings of non-linear imaging [5,6]. It is very difficult to realistically simulate the non-linear propagation and often it is not understood why the non-linear images are better. Most of the time the improvements can not be reproduced in phantom studies, precluding a thorough understanding of non-linear propagation.

Simulation of linear ultrasound imaging has been very successful by use of the Field II program [7,8] and numerous research groups and companies are using the program. Simulation of non-linear imaging has been considerably more difficult. Several studies on non-linear ultrasound wave propagation and the simulation of this have been carried out by a number of research groups. Many of the studies numerically integrate the 3-dimensional KZK equation [9–14]. These equations are computationally demanding to solve and results have been reported only on single-element, often axisymmetric sources.

Another approach called the operator splitting method (OSM) [15–19], where the different effects are separated and included one at a time. This can be used to numerically solve the non-linear wave equation. Based on this method, one of the currently most popular non-linear ultrasound simulation software, called Abersim [20–23], in which the KZK equation [24,25] is derived from the Westervelt equation [26], is transformed into a Burgers' equation [27] using the OSM. Then the Burgers' equation is solved numerically to model the non-linear ultrasound fields in incremental steps.

The biggest drawback of using OSM and numerically solving the Burgers' equation is that the calculation time can easily become extremely long. For instance, to simulate the non-linear field for a 64-element linear array transducer with a center frequency of 5 MHz, the calculation time is up to an entire day using Abersim. Optimization of non-linear ultrasound imaging is quite hard with such a long time simulation.

A promising approach for non-linear simulation is the angular spectrum approach (ASA) [28–30]. Mathematically, it originates from Fourier optics [31–33]. The ASA has been widely used in the linear acoustic simulation [34–38] due to its rapid computation time. It was firstly introduced to the non-linear acoustics by Alais and Hennion [28], and afterwards modified and extended in non-linear ultrasound simulation for single-element transducers [39–41]. Here the field is calculated at a plane and then non-linearly propagated using the ASA. In this way, an analytical solution of the non-linear wave equation can be obtained with certain proper assumptions. The computation can be executed in one step, which makes the calculation speed much faster.

In an ultrasound imaging system, a short pulse is usually emitted from the transducer. This yields a high bandwidth signal, and calculation with a single temporal frequency is insufficient, since the ASA is originally derived from monochromatic fields. The main objective of the project is to extend the ASA for simulating the pulsed non-linear ultrasound field and based on the ASA and Field II, develop an accurate, fast and flexible non-linear ultrasound simulation program, which can be used to optimize the non-linear ultrasound imaging for array transducers.

The initial study is focused on the linear ultrasound simulation using the ASA, which can be found in Conference paper I (Appendix C.1), where a planar piston transducer is simulated using the ASA in combination with Field II. The comparison is made between the ASA and Field II for monochromatic fields. The ASA is expanded to pulsed ultrasound fields In Conference paper II (Appendix C.2) and Journal paper I (Appendix C.3). A 64-element array transducer is linearly simulated. The results for the simulated pulse in time domain have been presented and also compared with Field II in Conference paper II (Appendix C.2). The linear pulsed fields generated by a circular concave transducer with a diameter of 0.5 inch are simulated using the ASA and measured under water using a hydrophone. The results are compared and presented in (Appendix C.3).

The non-linear model using the ASA for the second harmonic field has been implemented in Conference paper III-IV (Appendix C.4, C.5). The simula-

tion using a linear array transducer is compared with results obtained by the released non-linear ultrasound simulation program - Abersim in Conference paper III (Appendix C.4). The under-water hydrophone measurement for the second harmonic field using a circular concave transducer with a diameter of 1 inch is made in Conference paper IV (Appendix C.4), where the comparison for the second harmonic fields between the measured and ASA simulated results is presented.

The ASA for simulating the pulsed second harmonic fields is presented in Journal paper II (Appendix C.6) and Conference abstract I (Appendix C.7) , where an exist BK transducer (BK8804, from BK Medical Aps) is simulated in the program. A good agreement is made between the results using the ASA and Abersim. The investigation shows that the ASA simulation is over 100 times faster than the Abersim. The ASA is implemented based on Field II, which can simulate array transducer with arbitrary geometry, focusing and excitation. The theory of ASA, for linear simulation is given in Journal paper I (Appendix C.3), and for non-linear (second harmonic) simulation can be found in Conference paper I (Appendix C.1), Conference paper IV (Appendix C.5) and Journal paper II (Appendix C.6). Finally, the theory of ASA and equations for super harmonic components are presented and derived in the dissertation.

Conference abstract II (Appendix C.8) describes a dual-stage harmonic imaging. This idea combines the synthetic aperture sequential beamforming and harmonic imaging to further improve the resolution of an image. The preliminary results of this investigation are also shown at the end of the dissertation.

1.1 Contributions

The total contributions of the study in the field of non-linear ultrasound propagation and imaging during my PhD project period include one submitted patent, two submitted journal articles, four published conference papers and two submitted conference abstracts as well as one co-authored conference paper and one co-authored submitted abstract. These are listed as follows.

Patent

- Jørgen Arendt Jensen, **Yigang Du** and Henrik Jensen "Harmonic ultrasound imaging using synthetic aperture sequential beamforming", submitted to *US patent*, 2011

Journal article

- **Yigang Du**, Henrik Jensen and Jørgen Arendt Jensen, "Angular spectrum approach for simulating pulsed ultrasound fields", submitted for publishing in *Ultrasonics - Elsevier*, 2011

- **Yigang Du**, Henrik Jensen and Jørgen Arendt Jensen, "Fast non-linear pulsed ultrasound field simulation using an angular spectrum approach", submitted for publishing in *Journal of the Acoustical Society of America*, 2011

Conference paper and abstract

- **Yigang Du** and Jørgen Arendt Jensen, "Feasibility of non-linear simulation for Field II using an angular spectrum approach", presented at *IEEE - Ultrasonics Symposium* in Beijing, China, 2008, pp. 1314-1317

- **Yigang Du**, Henrik Jensen and Jørgen Arendt Jensen, "Angular spectrum simulation of pulsed ultrasound fields", presented at *IEEE - Ultrasonics Symposium* in Rome, Italy, 2009, pp. 2379-2382

- **Yigang Du**, Henrik Jensen and Jørgen Arendt Jensen, "Simulation of second harmonic ultrasound fields", presented at *IEEE - Ultrasonics Symposium* in San Diego, California, USA, 2010

- **Yigang Du**, Henrik Jensen and Jørgen Arendt Jensen, "Comparison of simulated and measured non-linear ultrasound fields", presented at *SPIE - Medical Imaging* in Orlando, Florida, USA, 2011, vol. 79680P, pp. 1-10

- **Yigang Du**, Henrik Jensen and Jørgen Arendt Jensen, "Angular spectrum approach for fast simulation of pulsed non-linear ultrasound fields", abstract submitted to *IEEE - Ultrasonics Symposium* in Orlando, Florida, USA, 2011

- **Yigang Du**, Joachim Rasmussen, Henrik Jensen and Jørgen Arendt Jensen, "Second harmonic imaging using synthetic aperture sequential beamforming", abstract submitted to *IEEE - Ultrasonics Symposium* in Orlando, Florida, USA, 2011

Co-authored paper and abstract

- Joachim Rasmussen, **Yigang Du** and Jørgen Arendt Jensen, "Non-linear imaging using an experimental synthetic aperture real time ultrasound scanner", presented at *Nordic Baltic Conference on Biomedical Engineering and Medical Physics* in Aalborg, Denmark, 2011

- Joachim Rasmussen, **Yigang Du**, Jens Munk Hansen, Martin Hemmsen and Jørgen Arendt Jensen, "Third harmonic imaging using a pulse inversion technique", abstract submitted to *IEEE - Ultrasonics Symposium* in Orlando, Florida, USA, 2011

1.2 Structure of the Dissertation

The specific description of each chapter is as follows.

Chapter 2 introduces the theory of modeling the non-linear wave equations and its solution using the ASA.

Chapter 3 presents the implementation of the ASA solution to the pulsed non-linear ultrasound fields.

Chapter 4 presents the non-linear simulation results using a linear array transducer. The results are generated by the ASA based on Field II and compared with the Abersim simulation results. (referred to Journal paper II, Appendix C.6 and Conference abstract I, Appendix C.7)

Chapter 5 presents the simulated and measured results from two geometrical focused piston transducers. (referred to Journal paper I, Appendix C.3 and Conference paper IV, Appendix C.5)

Chapter 6 derives the solutions for non-linear wave propagation and super harmonic components using the ASA.

Chapter 7 presents harmonic imaging using a dual-stage synthetic aperture sequential beamforming. (referred to Conference abstract II, Appendix C.8)

Chapter 8 concludes the theory and results presented in this dissertation.

Appendix A gives the detailed equation derivations of the intermediate steps for some complicated equations.

Appendix B shows some supplemental figures for Chapter 4. The figures are generated by Abersim.

Appendix C attaches the first author publications, which include 4 published conference papers, 2 submitted journal papers and 2 submitted conference abstracts.

CHAPTER

TWO

Theory

The theory of modeling non-linear acoustic fields is explained in this chapter. The linear and non-linear wave equations are derived, and then the solutions for both monochromatic and pulsed fields using the ASA are presented.

2.1 Linear and non-linear wave equations

The linear wave equation is derived from the state equation, continuity equation, and Euler force equation [42], which are expressed as follows.

State equation

$$\frac{P_i}{P_e} = \left(\frac{\rho}{\rho_0}\right)^{\gamma}, \tag{2.1}$$

where

P_i: medium instantaneous pressure
P_e: medium equilibrium pressure
ρ: medium instantaneous density
ρ_0: medium equilibrium density
γ: ratio of specific heats

This describes the acoustic behavior for the perfect gas under adiabatic conditions by the Thermodynamic Law.

Continuity equation

$$\frac{\partial \rho}{\partial t} + \nabla \cdot (\rho \vec{u}) = 0, \tag{2.2}$$

where

$\vec{u}$: particle velocity of a fluid element

t: time

This is the exact continuity equation derived by the Mass Conservation Law.

Euler force equation

$$\rho_0 \frac{\partial \vec{u}}{\partial t} + \nabla p = 0, \tag{2.3}$$

where

p: acoustic pressure given by

$$p = P_i - P_e. \tag{2.4}$$

This is the linear Euler's equation, which originates from Newton's Second Law with assumptions that the amplitude of the acoustic pressure is small enough so that the particle velocity is much smaller than the propagation speed of sound.

The solution to (2.1) can be found using a Taylor's expansion

$$P_i = P_e + \left(\frac{\partial P_i}{\partial \rho}\right)_{\rho_0} (\rho - \rho_0) + \frac{1}{2}\left(\frac{\partial^2 P_i}{\partial \rho^2}\right)_{\rho_0} (\rho - \rho_0)^2 + \cdots \tag{2.5}$$

For small amplitude acoustic pressure, only the first order partial derivative term of the Taylor's expansion is taken into consideration. Here the condensation s is introduced by

$$s = \frac{\rho - \rho_0}{\rho_0}. \tag{2.6}$$

For a small condensation due to the small amplitude, (2.2) simplifies to

$$\frac{\partial s}{\partial t} + \nabla \cdot \vec{u} = 0. \tag{2.7}$$

On the other hand, by substituting (2.1) into (2.5) for the first order term and using (2.4) and (2.6), the Taylor's expansion (2.5) is rewritten as

$$p = P_e \gamma s. \tag{2.8}$$

Finally, combining (2.3), (2.7) and (2.8) gives

$$\nabla^2 p - \frac{1}{c_0^2}\frac{\partial^2 p}{\partial t^2} = 0, \tag{2.9}$$

where

c_0: sound speed given by

$$c_0 = \sqrt{P_e \gamma / \rho_0}. \tag{2.10}$$

This is the well-know linear lossless wave equation, which describes the change of the acoustic pressure as a function of space and time for a constant speed of sound.

For a high amplitude acoustic pressure, the higher order partial derivative terms of the Taylor's expansion should be considered. Thus, by use of the exact continuity equation (2.2), a non-linear wave equation can be derived. For example, if the second-order partial derivative term in Taylor's expansion is involved, substituting (2.1) into (2.5) with the first and second order terms, the Taylor's expansion can be transformed as

$$P_i - P_e = P_e \gamma \left(\frac{\rho - \rho_0}{\rho_0} \right) + \frac{1}{2} P_e \gamma (\gamma - 1) \left(\frac{\rho - \rho_0}{\rho_0} \right)^2, \tag{2.11}$$

by use of (2.4) and (2.6), (2.11) can be expressed by

$$p = P_e \gamma s + \frac{1}{2} P_e \gamma (\gamma - 1) s^2. \tag{2.12}$$

The second term of the right hand side of (2.12) contains a s^2, which can be replaced by use of (2.8) since s is still a small number (pretty much lower than 1) even for relatively high amplitude acoustic pressure.

$$p = P_e \gamma s + \frac{1}{2} (\gamma - 1) \frac{p^2}{P_e \gamma}, \tag{2.13}$$

by use of (2.10), finally, (2.13) can be written by

$$s = \frac{p}{\rho_0 c_0^2} - \frac{1}{2} (\gamma - 1) \frac{p^2}{\rho_0^2 c_0^4}. \tag{2.14}$$

For plane waves, the specific acoustic impedance z is defined as

$$z = p/u = \rho_0 c_0. \tag{2.15}$$

By use of (2.15), the Euler's equation (2.3) is transformed as

$$\nabla p + \frac{1}{c_0} \frac{\partial p}{\partial t} = 0, \tag{2.16}$$

by use of (2.6) and (2.15), the continuity equation (2.2) is transformed as

$$\frac{\partial s}{\partial t} + \frac{1}{\rho_0 c_0} \nabla p + \frac{1}{\rho_0 c_0} \nabla p s = 0, \tag{2.17}$$

by use of (2.8), ps in the last term of the left hand side of (2.16) can be expressed as

$$ps = P_e \gamma s^2, \tag{2.18}$$

substituting (2.18) into (2.17) gives to

$$\frac{\partial s}{\partial t} + \frac{1}{\rho_0 c_0}\nabla p + \frac{P_e \gamma}{\rho_0 c_0}\nabla s^2 = 0, \tag{2.19}$$

by use of (2.14), s^2 in the last term of the left hand side of (2.19) can be expressed as

$$s^2 = \frac{p^2}{\rho_0^2 c_0^4}. \tag{2.20}$$

The p^3 and p^4 are ignored since they are much smaller compared to p and p^2. Substituting (2.20) into (2.16) and by use of (2.10), the transformed continuity equation (2.19) can be rewritten by

$$\frac{\partial s}{\partial t} + \frac{1}{\rho_0 c_0}\nabla p + \frac{1}{\rho_0^2 c_0^3}\nabla p^2 = 0. \tag{2.21}$$

Rewrite (2.16) as

$$\nabla p^2 = -\frac{1}{c_0}\frac{\partial p^2}{\partial t}, \tag{2.22}$$

substituting (2.22) into (2.21) gives to

$$\frac{\partial s}{\partial t} + \frac{1}{\rho_0 c_0}\nabla p - \frac{1}{\rho_0^2 c_0^4}\frac{\partial p^2}{\partial t} = 0. \tag{2.23}$$

Taking derivative for (2.16) with respect to space and for (2.23) with respect to time results in

$$\nabla^2 p + \frac{1}{c_0}\nabla\frac{\partial p}{\partial t} = 0, \tag{2.24}$$

$$\frac{\partial^2 s}{\partial t^2} + \frac{1}{\rho_0 c_0}\nabla\frac{\partial p}{\partial t} - \frac{1}{\rho_0^2 c_0^4}\frac{\partial^2 p^2}{\partial t^2} = 0. \tag{2.25}$$

Multiplying (2.24) by $1/\rho_0$ and subtracting by (2.25) gives to

$$\frac{\partial^2 s}{\partial t^2} - \frac{1}{\rho_0}\nabla^2 p - \frac{1}{\rho_0^2 c_0^4}\frac{\partial^2 p^2}{\partial t^2} = 0, \tag{2.26}$$

substituting (2.14) into (2.26) results in

$$\frac{1}{\rho_0 c_0^2}\frac{\partial^2 p}{\partial t^2} - \frac{(\gamma - 1)}{2\rho_0^2 c_0^4}\frac{\partial^2 p^2}{\partial t^2} - \frac{1}{\rho_0}\nabla^2 p - \frac{1}{\rho_0^2 c_0^4}\frac{\partial^2 p^2}{\partial t^2} = 0, \tag{2.27}$$

multiplying (2.27) by ρ_0 and combining the second and fourth terms of the left hand side of (2.27) gives to

$$\left(\nabla^2 - \frac{1}{c_0^2}\frac{\partial^2}{\partial t^2}\right) p = -\frac{\beta}{\rho_0 c_0^4}\frac{\partial^2 p^2}{\partial t^2}, \tag{2.28}$$

where

β: coefficient of nonlinearity given by

$$\beta = (\gamma + 1)/2. \tag{2.29}$$

Thus, (2.28) is the so-called lossless Westervelt equation [26], which is used to model the non-linear ultrasound propagation.

2.2 Solution to linear and non-linear wave equations

It is assumed that the total sound pressure after propagation is the sum of the fundamental component and its corresponding second harmonic component and the former is much larger than the latter. These can be expressed as

$$p \approx p_1 + p_2 \tag{2.30}$$

$$p_1 \gg p_2. \tag{2.31}$$

where

p_1: fundamental component of the acoustic pressure
p_2: second harmonic component of the acoustic pressure

Using a separate variable solution [40–42] (described in Appendix A.1), the acoustic pressure of the nth harmonic is

$$p_n(x, y, z, t) = \frac{1}{2} P_n(x, y, z) e^{-jn\omega t} + c.c., \qquad n = 1, 2 \tag{2.32}$$

where

P_n: amplitude of the sound wave of the nth harmonic
ω: fundamental angular frequency
$c.c.$: complex conjugate of the preceding term given by

$$c.c. = \left(\frac{1}{2} P_n(x, y, z) e^{-jn\omega t}\right)^*. \tag{2.33}$$

The coefficient of $P_n(x, y, z)$ - $1/2$ makes the total energy remain the same after summing with $c.c.$. Substituting (2.30) and (2.32) without $c.c.$ into (2.28) leads to

$$(\nabla^2 + k^2) P_1 e^{-j\omega t} + (\nabla^2 + 4k^2) P_2 e^{-2j\omega t} = \frac{2\beta k^2}{\rho_0 c_0^2} P_1^2 e^{-2j\omega t}, \tag{2.34}$$

where

k: wave number given by

$$k = \omega / c_0. \tag{2.35}$$

P_1^2 in (2.34) is obtained using the assumption from (2.31), $p_1 \gg p_2 \Longrightarrow (p_1 + p_2)^2 \approx p_1^2$. Thus, (2.34) can be divided into two equations, since the first term of the left hand side of (2.34) after the cancellation of the exponential term $e^{-j\omega t}$ from both sides, is not a function of time t.

$$(\nabla^2 + k^2)P_1 = 0, \tag{2.36}$$

$$(\nabla^2 + 4k^2)P_2 = \frac{2\beta k^2}{\rho_0 c_0^2} P_1^2. \tag{2.37}$$

Here, the solutions to the two equations can be separately derived by the ASA, where the linear ASA is used to solve the Helmholtz equation (2.36), which is described in the following section, and non-linear ASA is applied to derive the implementable solution to (2.37) afterwards.

2.2.1 ASA for solving the linear wave equation

The angular spectrum of the acoustic pressure is defined by

$$\hat{P}(k_x, k_y, z) = \iint_{-\infty}^{\infty} P(x, y, z) e^{-j(k_x x + k_y y)} dx dy, \tag{2.38}$$

$\hat{P}(k_x, k_y, z)$ is the angular spectrum as well as two-dimensional spatial Fourier transform of $P(x, y, z)$, which can be given by the inverse Fourier transform by

$$P(x, y, z) = \frac{1}{(2\pi)^2} \iint_{-\infty}^{\infty} \hat{P}(k_x, k_y, z) e^{j(k_x x + k_y y)} dk_x dk_y. \tag{2.39}$$

Substituting (2.39) into (2.36) gives to

$$(\nabla^2 + k^2) \iint_{-\infty}^{\infty} \hat{P}(k_x, k_y, z) e^{j(k_x x + k_y y)} dk_x dk_y = 0. \tag{2.40}$$

Eliminating the integral operation, (2.40) can be expressed by

$$\left(\frac{\partial^2}{\partial x^2} + \frac{\partial^2}{\partial y^2} + \frac{\partial^2}{\partial z^2} + k^2 \right) \hat{P}(k_x, k_y, z) e^{j(k_x x + k_y y)} = 0. \tag{2.41}$$

Taking the derivative with respect to x, y and z will give to

$$\left((jk_x)^2 + (jk_y)^2 + \frac{\partial^2}{\partial z^2} + k^2\right)\hat{P}(k_x, k_y, z)e^{j(k_x x + k_y y)} = 0. \tag{2.42}$$

Eliminating the exponential term, (2.42) is recombined by

$$\frac{d^2}{dz^2}\hat{P}(k_x, k_y, z) + k_z^2\hat{P}(k_x, k_y, z) = 0, \tag{2.43}$$

where

$$k_z^2 = k^2 - k_x^2 - k_y^2. \tag{2.44}$$

Thus, (2.43) is a second-order ordinary differential equation. By assuming that the acoustic wave propagates along $+z$ direction as shown in Fig. 2.1, the solution can be found by

$$\hat{P}(k_x, k_y, z) = \begin{cases} Ae^{-jz\sqrt{k^2 - k_x^2 - k_y^2}}, & k^2 > k_x^2 + k_y^2 \\ Be^{-z\sqrt{k_x^2 + k_y^2 - k^2}}, & k^2 \leq k_x^2 + k_y^2 \end{cases} \tag{2.45}$$

where A and B are amplitudes of the acoustic wave. The evanescent wave will appear due to the propagation phenomenon of plane waves when the second condition in (2.45) is satisfied. Thus, the angular spectrums at $z = z_0$ and $z = z_1$ can be expressed by

$$\hat{P}_0(k_x, k_y, z_0) = \begin{cases} Ae^{-jz_0\sqrt{k^2 - k_x^2 - k_y^2}}, & k^2 > k_x^2 + k_y^2 \\ Be^{-z_0\sqrt{k_x^2 + k_y^2 - k^2}}, & k^2 \leq k_x^2 + k_y^2 \end{cases} \tag{2.46}$$

$$\hat{P}_1(k_x, k_y, z_1) = \begin{cases} Ae^{-jz_1\sqrt{k^2 - k_x^2 - k_y^2}}, & k^2 > k_x^2 + k_y^2 \\ Be^{-z_1\sqrt{k_x^2 + k_y^2 - k^2}}, & k^2 \leq k_x^2 + k_y^2. \end{cases} \tag{2.47}$$

Finally, the ASA solution to (2.36) is obtained by dividing (2.46) by (2.47)

$$\hat{P}_1(k_x, k_y, z_1) = \begin{cases} \hat{P}_0(k_x, k_y, z_0)e^{-j(z_1 - z_0)\sqrt{k^2 - k_x^2 - k_y^2}}, & k^2 > k_x^2 + k_y^2, \\ \hat{P}_0(k_x, k_y, z_0)e^{-(z_1 - z_0)\sqrt{k_x^2 + k_y^2 - k^2}}, & k^2 \leq k_x^2 + k_y^2, \end{cases} \tag{2.48}$$

where $P_1(x, y, z_1)$ in (2.36) can be found by (2.39) and $P_0(k_x, k_y, z_0)$ in (2.48) can be obtained by (2.38). Thus P_0 and P_1 can be thought of as two planes in x-y plane at fixed z_0 and z_1 as shown in Fig. 2.1. k_x and k_y are the transverse wave numbers along x and y directions.

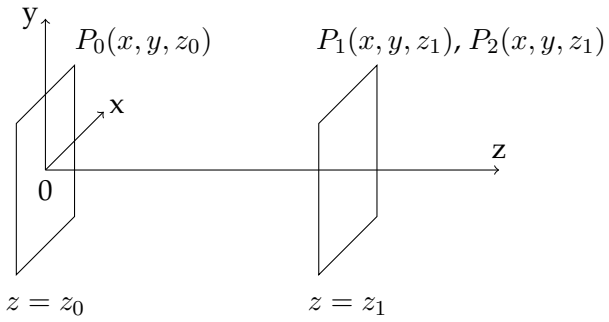

Figure 2.1: Schematic view of the angular spectrum approach - The acoustic plane at z_0 is the source plane, and the acoustic plane at z_1 is the calculated plane. P_1 is the fundamental component and P_2 is the second harmonic component.

2.2.2 ASA for solving the non-linear wave equation

To solve (2.37), the convolution theorem [43, 44] is introduced by

$$f \cdot g = \mathcal{F}^{-1}\left\{\mathcal{F}\{f\} * \mathcal{F}\{g\}\right\}, \tag{2.49}$$

P_1^2 in (2.37) is the square of the pressure in spatial domain. This can be expressed as the inverse spatial Fourier transform of its convolution in spatial frequency domain according to the convolution theorem. By use of (2.49), (2.37) can be rewritten as

$$\begin{aligned}(\nabla^2 + 4k^2)P_2 \quad = \quad & \mathcal{F}^{-1}\left\{\frac{\beta k^2}{2\pi^2 \rho_0 c_0^2}\iint \hat{P}_1(k_x', k_y', z_1)\right. \\ & \left.\times \hat{P}_1(k_x - k_x', k_y - k_y', z_1)dk_x'dk_y'\right\}. \end{aligned} \tag{2.50}$$

An ordinary differential equation with an inhomogeneous integral term is obtained after the 2D (x-y) spatial Fourier transform on both sides of (2.50), with the help of (2.48) under the conditions of $k^2 > (k_x')^2 + (k_y')^2$ and $k^2 > (k_x - k_x')^2 + (k_y - k_y')^2$ (see Appendix A.2 for details)

$$\left(\frac{d^2}{dz^2} + k_{z2}^2\right)\hat{P}_2(k_x, k_y, z_1) = \frac{\beta k^2}{2\pi^2 \rho_0 c_0^2} M(k_x, k_y, z_1), \tag{2.51}$$

where

$$
\begin{aligned}
M(k_x, k_y, z_1) &= \iint e^{-j(z_1-z_0)(k_z'+k_z'')} \hat{P}_0(k_x', k_y', z_0) \\
&\quad \times \hat{P}_0(k_x - k_x', k_y - k_y', z_0) dk_x' dk_y', \qquad (2.52) \\
k_{z2} &= \sqrt{4k^2 - k_x^2 - k_y^2}, \qquad (2.53) \\
k_z' &= \sqrt{k^2 - (k_x')^2 - (k_y')^2}, \qquad (2.54) \\
k_z'' &= \sqrt{k^2 - (k_x - k_x')^2 - (k_y - k_y')^2}. \qquad (2.55)
\end{aligned}
$$

The solution to (2.51) is given by [40, 45–48] (see Appendix A.3 for details)

$$
\begin{aligned}
\hat{P}_2(k_x, k_y, z_1) &= \frac{\beta k^2}{2\pi^2 \rho_0 c_0^2} \iint \frac{e^{-j(z_1-z_0)(k_z'+k_z'')} - e^{-j(z_1-z_0)k_{z2}}}{k_{z2}^2 - (k_z' + k_z'')^2} \hat{P}_0(k_x', k_y', z_0) \\
&\quad \times \hat{P}_0(k_x - k_x', k_y - k_y', z_0) dk_x' dk_y', \qquad (2.56) \\
&\text{when} \quad 4k^2 > k_x^2 + k_y^2, \;\; k^2 > (k_x')^2 + (k_y')^2, \\
&\quad k^2 > (k_x - k_x')^2 + (k_y - k_y')^2.
\end{aligned}
$$

Three conditions with each of them having two cases give rise to eight cases in total. An example using the similar derivations under the conditions of $4k^2 \leq k_x^2 + k_y^2$, $k^2 \leq (k_x')^2 + (k_y')^2$ and $k^2 \leq (k_x - k_x')^2 + (k_y - k_y')^2$, is given by

$$
\begin{aligned}
\hat{P}_2(k_x, k_y, z_1) &= \frac{\beta k^2}{2\pi^2 \rho_0 c_0^2} \iint \frac{e^{-(z_1-z_0)(k_z'+k_z'')} - e^{-(z_1-z_0)k_{z2}}}{k_{z2}^2 - (k_z' + k_z'')^2} \hat{P}_0(k_x', k_y', z_0) \\
&\quad \times \hat{P}_0(k_x - k_x', k_y - k_y', z_0) dk_x' dk_y', \qquad (2.57) \\
&\text{when} \quad 4k^2 \leq k_x^2 + k_y^2, \;\; k^2 \leq (k_x')^2 + (k_y')^2, \\
&\quad k^2 \leq (k_x - k_x')^2 + (k_y - k_y')^2.
\end{aligned}
$$

There will be eight equations under different conditions, (2.56) and (2.57) are two of them as examples. These are the solution to the Westervelt equation using the ASA and the wave number k in (2.56) or (2.57) is a constant, which is used for monochromatic fields.

2.2.3 ASA for calculating pulsed acoustic fields

To simulate pulsed ultrasound fields, $\hat{P}_0$, $\hat{P}_1$ and $\hat{P}_2$ should be a function of the temporal frequency f. The fundamental component $\hat{P}_1$ has two cases and

given by

$$\hat{P}_1(k_x,k_y,z_1,f)=\begin{cases}\hat{P}_0(k_x,k_y,z_0,f)e^{-\frac{f}{|f|}j(z_1-z_0)\sqrt{k^2-k_x^2-k_y^2}}, & k^2>k_x^2+k_y^2,\\ \hat{P}_0(k_x,k_y,z_0,f)e^{-(z_1-z_0)\sqrt{k_x^2+k_y^2-k^2}}, & k^2\le k_x^2+k_y^2.\end{cases} \tag{2.58}$$

The second harmonic component $\hat{P}_2$, under different conditions, has eight cases, which can be further divided into two parts with two conditions. Under the condition of $4k^2>k_x^2+k_y^2$, $\hat{P}_2$ has four cases and given by

$$\hat{P}_2(k_x,k_y,z_1,2f) = \begin{cases}\frac{2\beta f^2}{\rho_0 c_0^4}\iint\frac{e^{-\frac{f}{|f|}j(z_1-z_0)(k_z'+k_z'')}-e^{-\frac{f}{|f|}j(z_1-z_0)k_{z2}}}{k_{z2}^2-(k_z'+k_z'')^2}\\ \times\hat{P}_0(k_x',k_y',z_0,f)\hat{P}_0(k_x-k_x',k_y-k_y',z_0,f)dk_x'dk_y',\\ \text{when}\quad k^2>(k_x')^2+(k_y')^2,\\ \qquad k^2>(k_x-k_x')^2+(k_y-k_y')^2,\\ \\ \frac{2\beta f^2}{\rho_0 c_0^4}\iint\frac{e^{-(z_1-z_0)\left(\frac{f}{|f|}jk_z'+k_z''\right)}-e^{-\frac{f}{|f|}j(z_1-z_0)k_{z2}}}{k_{z2}^2-(k_z'+k_z'')^2}\\ \times\hat{P}_0(k_x',k_y',z_0,f)\hat{P}_0(k_x-k_x',k_y-k_y',z_0,f)dk_x'dk_y',\\ \text{when}\quad k^2>(k_x')^2+(k_y')^2,\\ \qquad k^2\le(k_x-k_x')^2+(k_y-k_y')^2,\\ \\ \frac{2\beta f^2}{\rho_0 c_0^4}\iint\frac{e^{-(z_1-z_0)\left(k_z'+\frac{f}{|f|}jk_z''\right)}-e^{-\frac{f}{|f|}j(z_1-z_0)k_{z2}}}{k_{z2}^2-(k_z'+k_z'')^2}\\ \times\hat{P}_0(k_x',k_y',z_0,f)\hat{P}_0(k_x-k_x',k_y-k_y',z_0,f)dk_x'dk_y',\\ \text{when}\quad k^2\le(k_x')^2+(k_y')^2,\\ \qquad k^2>(k_x-k_x')^2+(k_y-k_y')^2,\\ \\ \frac{2\beta f^2}{\rho_0 c_0^4}\iint\frac{e^{-(z_1-z_0)(k_z'+k_z'')}-e^{-\frac{f}{|f|}j(z_1-z_0)k_{z2}}}{k_{z2}^2-(k_z'+k_z'')^2}\\ \times\hat{P}_0(k_x',k_y',z_0,f)\hat{P}_0(k_x-k_x',k_y-k_y',z_0,f)dk_x'dk_y',\\ \text{when}\quad k^2\le(k_x')^2+(k_y')^2,\\ \qquad k^2\le(k_x-k_x')^2+(k_y-k_y')^2,\end{cases}$$
$$\text{when}\qquad 4k^2>k_x^2+k_y^2. \tag{2.59}$$

Under the condition of $4k^2 \leq k_x^2 + k_y^2$, $\hat{P}_2$ has four cases and given by

$$
\hat{P}_2(k_x, k_y, z_1, 2f) = \begin{cases}
\frac{2\beta f^2}{\rho_0 c_0^4} \iint \frac{e^{-\frac{f}{|f|} j(z_1-z_0)(k_z'+k_z'')} - e^{-(z_1-z_0)k_{z2}}}{k_{z2}^2 - (k_z'+k_z'')^2} \\
\times \hat{P}_0(k_x', k_y', z_0, f) \hat{P}_0(k_x - k_x', k_y - k_y', z_0, f) dk_x' dk_y', \\
\text{when} \quad k^2 > (k_x')^2 + (k_y')^2, \\
\qquad\quad k^2 > (k_x - k_x')^2 + (k_y - k_y')^2, \\
\\
\frac{2\beta f^2}{\rho_0 c_0^4} \iint \frac{e^{-(z_1-z_0)\left(\frac{f}{|f|} j k_z' + k_z''\right)} - e^{-(z_1-z_0)k_{z2}}}{k_{z2}^2 - (k_z'+k_z'')^2} \\
\times \hat{P}_0(k_x', k_y', z_0, f) \hat{P}_0(k_x - k_x', k_y - k_y', z_0, f) dk_x' dk_y', \\
\text{when} \quad k^2 > (k_x')^2 + (k_y')^2, \\
\qquad\quad k^2 \leq (k_x - k_x')^2 + (k_y - k_y')^2, \\
\\
\frac{2\beta f^2}{\rho_0 c_0^4} \iint \frac{e^{-(z_1-z_0)\left(k_z' + \frac{f}{|f|} j k_z''\right)} - e^{-(z_1-z_0)k_{z2}}}{k_{z2}^2 - (k_z'+k_z'')^2} \\
\times \hat{P}_0(k_x', k_y', z_0, f) \hat{P}_0(k_x - k_x', k_y - k_y', z_0, f) dk_x' dk_y', \\
\text{when} \quad k^2 \leq (k_x')^2 + (k_y')^2, \\
\qquad\quad k^2 > (k_x - k_x')^2 + (k_y - k_y')^2, \\
\\
\frac{2\beta f^2}{\rho_0 c_0^4} \iint \frac{e^{-(z_1-z_0)(k_z'+k_z'')} - e^{-(z_1-z_0)k_{z2}}}{k_{z2}^2 - (k_z'+k_z'')^2} \\
\times \hat{P}_0(k_x', k_y', z_0, f) \hat{P}_0(k_x - k_x', k_y - k_y', z_0, f) dk_x' dk_y', \\
\text{when} \quad k^2 \leq (k_x')^2 + (k_y')^2, \\
\qquad\quad k^2 \leq (k_x - k_x')^2 + (k_y - k_y')^2,
\end{cases}
$$

$$
\text{when} \qquad 4k^2 \leq k_x^2 + k_y^2. \tag{2.60}
$$

The wave number k in (2.56) or (2.57) is replaced by $k = 2\pi f/c_0$ in (2.59) and (2.60) since it is no longer a constant and varies with the frequency f. Thus, the relations between the fundamental and second harmonic fields at the plane $z = z_1$, and the acoustic source at the plane $z = z_0$ are found by (2.58), (2.59) and (2.60), respectively. The fundamental and second harmonic pressure in space and time domain can be obtained by the 3D (1D for tempo-

ral frequency and 2D for k-space on x-y plane) inverse Fourier transform

$$p_1(x,y,z_1,t) = \frac{1}{(2\pi)^2}\iiint_{-\infty}^{\infty} \hat{P}_1(k_x,k_y,z_1,f)e^{j(k_x x+k_y y+2\pi ft)}dk_x dk_y df, \tag{2.61}$$

$$p_2(x,y,z_1,t) = \frac{1}{(2\pi)^2}\iiint_{-\infty}^{\infty} \hat{P}_2(k_x,k_y,z_1,2f)e^{j(k_x x+k_y y+2\pi ft)}dk_x dk_y df. \tag{2.62}$$

The acoustic source $\hat{P}_0(k_x,k_y,z_0,f)$ in (2.58), (2.59) and (2.60) is calculated by the 3D (1D for time and 2D for space on x-y plane) Fourier transform

$$\hat{P}_0(k_x,k_y,z_0,f) = \iiint_{-\infty}^{\infty} p_0(x,y,z_0,t)e^{-j(k_x x+k_y y+2\pi ft)}dxdydt. \tag{2.63}$$

By use of (2.58), (2.59), (2.60), (2.61), (2.62) and (2.63), finally, the fundamental pressure $p_1(x,y,z_1,t)$ and second harmonic pressure $p_2(x,y,z_1,t)$ in time domain can be calculated as long as the source pressure $p_0(x,y,z_0,t)$ and the distance between two planes $z_1 - z_0$ are known. This is the full theory of the ASA for solving the non-linear wave equation and calculating the second harmonic components for pulsed acoustic fields.

CHAPTER

THREE

Implementation of the ASA

This chapter presents the implementation of the linear and non-linear ASA used for simulating the pulsed ultrasound fields. The discrete forms of (2.58) for the linear ASA, and (2.59) and (2.60) for the non-linear ASA will be implemented in Matlab. The variables in their discrete forms from (2.58), (2.59) and (2.60) are written by

$$\begin{aligned}
\hat{P}_0(k'_x, k'_y, z_0, f) &\rightarrow \hat{P}_{d_0}(n_x, n_y, n_f), \\
\hat{P}_0(k_x - k'_x, k_y - k'_y, z_0, f) &\rightarrow \hat{P}_{d_0}(m_x - n_x, m_y - n_y, n_f), \\
\hat{P}_1(k_x, k_y, z_1, f) &\rightarrow \hat{P}_{d_1}(n_x, n_y, n_f), \\
\hat{P}_2(k_x, k_y, z_1, 2f) &\rightarrow \hat{P}_{d_2}(m_x, m_y, n_{2f}).
\end{aligned}$$

One temporal frequency component is selected at one computation from $\hat{P}_0(k'_x, k'_y, z_0, f)$, which is calculated by (2.63). $p_0(x, y, z_0, t)$ in (2.63) is the source for the ASA and is simulated by Field II using the function calc_hp [49]. The variable z_0 should not be zero due to the singularity at $z_0 = 0$ when Field II is used. To satisfy the previous assumption from (A.48), z_0 is supposed to be close to the transducer surface. $z_0 = 1$ mm is used in the implementation, so that the non-linear effect in $p_0(x, y, z_0, t)$ can be ignored, since a propagation distance of 1 mm is too small to generate a non-linear pulse.

The spatial sampling frequency at x-y plane is given as k_s and the temporal sampling frequency is f_s. The sampling range in spatial frequency domain is $[-\frac{k_s}{2}, \frac{k_s}{2})$ and in temporal frequency domain is $[-\frac{f_s}{2}, \frac{f_s}{2})$.

3.1 Implementing equations for linear ASA

For linear ASA, the fundamental component is calculated by implementing the discrete form of (2.58), which is given by

$$\hat{P}_{d_1}(n_x,n_y,n_f)=\begin{cases}\hat{P}_{d_0}(n_x,n_y,n_f)e^{j(z_1-z_0)\sqrt{k^2-k_x^2(n_x)-k_y^2(n_y)}},\\ \text{when}\quad f<0, k^2>k_x^2(n_x)+k_y^2(n_y),\\ \\ \hat{P}_{d_0}(n_x,n_y,n_f)e^{-j(z_1-z_0)\sqrt{k^2-k_x^2(n_x)-k_y^2(n_y)}},\\ \text{when}\quad f>0, k^2>k_x^2(n_x)+k_y^2(n_y),\\ \\ \hat{P}_{d_0}(n_x,n_y,n_f)e^{-(z_1-z_0)\sqrt{k_x^2(n_x)+k_y^2(n_y)-k^2}},\\ \text{when}\quad k^2\le k_x^2(n_x)+k_y^2(n_y).\end{cases} \tag{3.1}$$

The fundamental pulse $p_1(x,y,z_1,t)$ can be calculated by applying (2.61) to $\hat{P}_{d_1}(n_x,n_y,n_f)$. The Matlab functions fft, ifft, fft2 and ifft2 are used for the three-dimensional forward and inverse Fourier transforms (2.61) and (2.63).

3.2 Implementing equations for non-linear ASA

For non-linear ASA, the double integral term of (2.59) is rewritten in discrete form by

$$\begin{aligned}\mathrm{DI}(m_x,m_y,n_f)=\frac{1}{N_xN_y}\sum_{n_y=0}^{N_y-1}\sum_{n_x=0}^{N_x-1}\hat{P}_{d_0}(n_x,n_y,n_f)\hat{P}_{d_0}(m_x-n_x,m_y-n_y,n_f)\\ \times\frac{e^{-j(z_1-z_0)[k_z'(n_x,n_y)+k_z''(m_x-n_x,m_y-n_y)]}-e^{-j(z_1-z_0)k_{z2}(m_x,m_y)}}{k_{z2}^2(m_x,m_y)-[k_z'(n_x,n_y)+k_z''(m_x-n_x,m_y-n_y)]^2},\\ (m_x=0,\ldots M_x-1,\qquad m_y=0,\ldots M_y-1)\end{aligned} \tag{3.2}$$

where

$$k_{z2}(m_x,m_y) = \sqrt{4k^2-k_x^2(m_x)-k_y^2(m_y)}, \tag{3.3}$$

$$k_z'(n_x,n_y) = \sqrt{k^2-k_x'^2(n_x)-k_y'^2(n_y)}, \tag{3.4}$$

$$k_z''(m_x-n_x,m_y-n_y) = \sqrt{k^2-[k_x(m_x)-k_x'(n_x)]^2-[k_y(m_y)-k_y'(n_y)]^2}. \tag{3.5}$$

DI is the discrete form of the double integral term in (2.59) at a fixed temporal frequency f, where $f > 0$, $4k^2 > k_x^2 + k_y^2$, $k^2 > (k_x')^2 + (k_y')^2$, $k^2 > (k_x - k_x')^2 + (k_y - k_y')^2$ and $k = 2\pi f/c_0$. The expression also depends on the sign of f. Hence, there will be totally 16 different discrete implementing equations and (3.2) is one of them. (see all discrete equations in Appendix A.4)

For finite series, $\hat{P}_{d_0}$ and k_z'' repeat themselves in the spatial frequency domain. This ensures that $\hat{P}_{d_0}(m_x - n_x, m_y - n_y, n_f)$ and $k_z''(m_x - n_x, m_y - n_y)$ have their repeated values when the index is less than 0 or larger than $N_x - 1$ or $N_y - 1$. This is presented in Fig. 3.1, where $\hat{P}_{d_0}(-1, -1, n_f) = \hat{P}_{d_0}(N_x - 1, N_y - 1, n_f)$ and $\hat{P}_{d_0}(N_x + 1, N_y + 1, n_f) = \hat{P}_{d_0}(1, 1, n_f)$, etc.

The second step is to take the multiplication of DI and the coefficient term before the double integral in (2.59). The frequency f should be the same as previously selected for DI. This can be expressed by

$$\hat{P}_{d_2}(m_x, m_y, n_{2f}) = \frac{2\beta f^2}{\rho_0 c_0^4} \mathrm{DI}(m_x, m_y, n_f). \tag{3.6}$$

$\hat{P}_{d_2}(m_x, m_y, n_{2f})$ is the second harmonic component at the corresponding temporal frequency. By calculating each frequency for $\hat{P}_{d_2}$, the second harmonic components in a certain bandwidth are found at the plane $z = z_1$ as shown in Fig. 2.1. Applying (2.62), the second harmonic pulse $p_2(x, y, z_1, t)$ can finally be obtained. The Matlab functions fft, ifft, fft2 and ifft2 are used for the three-dimensional forward and inverse Fourier transforms (2.62) and (2.63).

3.3 Parameters selection and conclusion

To successfully simulate the non-linear ultrasound propagation, the proper parameters have to be selected in the implementation. First of all, the virtual source used in the ASA is very close to but not the real source, which is simulated by Field II. The ASA source plane has to be large enough to cover all the acoustic waves propagating from the previous source. Therefore, the size of the ASA source plane should match that of the transducer selected from Field II. Generally speaking, the ASA source is 10% to 20% larger than the size of the transducer simulated by Field II. The acoustic wave, energy or power at the ASA source plane can also be calculated linearly using Field II since the propagation distance is small that giving no non-linear effect. Then

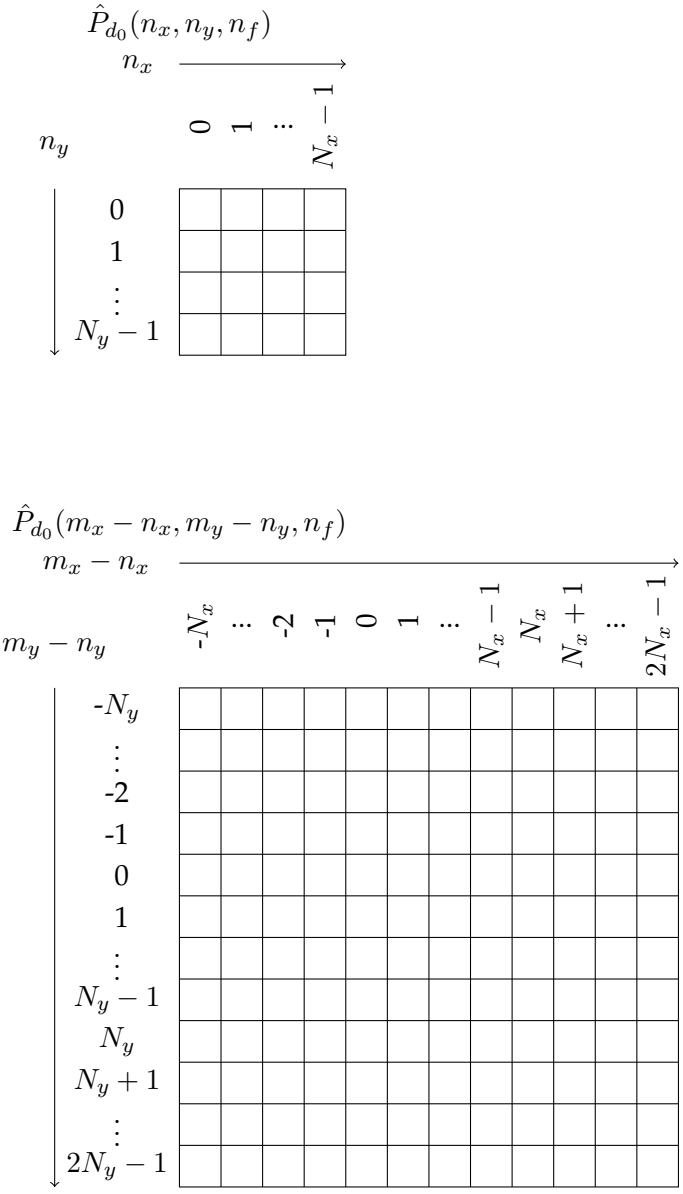

Figure 3.1: Schematic view of the implementation - $\hat{P}_{d_0}(n_x, n_y, n_f)$ is shown at the top of the figure and $\hat{P}_{d_0}(m_x - n_x, m_y - n_y, n_f)$ is shown with its index numbers at the bottom. The value of $\hat{P}_{d_0}(m_x - n_x, m_y - n_y, n_f)$ will repeat when the index number lower than 0 or larger than $N_x - 1$ or $N_y - 1$, for example $\hat{P}_{d_0}(-N_x, -N_y, n_f) = \hat{P}_{d_0}(0, 0, n_f)$.

an appropriate ASA source size can also be selected and checked through the calculation.

The ASA source obtained by Field II has a number of pulses in the time domain. The temporal sampling frequency f_s is chosen in Field II and usually $f_s = 100$ MHz for simulating a transducer with a center frequency around 4 MHz to 8 MHz. The spatial sampling frequency at the ASA source should satisfy Nyquist-Shannon Sampling Theorem [50], which says that the spatial interval between each two adjacent points should be less than a half wavelength.

Using the pulsed ASA based on Field II, a non-linear transmission field is simulated. The source of the ASA contains a set of temporal frequency components, which can simulate the high bandwidth harmonic signals. The source of the ASA is generated by Field II, which can simulate array transducers with any arbitrary geometry, focusing, excitation and apodization.

CHAPTER

FOUR

Results from a Linear Array Transducer

To investigate the implementation of the ASA for non-linear ultrasound fields, an instance of simulating a linear array transducer is described in this chapter. The transmission ultrasound fields for both the fundamental and second harmonic components are simulated using the ASA based on Field II. The non-linear simulation program - Abersim [20, 21], is used as the reference to compare with the simulation results from the ASA and Field II. The computation time of the Abersim and ASA for non-linear ultrasound fields is also presented.

4.1 Simulation setup

This section describes the specific parameters used in the simulation for the transducer and propagating medium, and setups of the assistant program, Field II and Abersim.

4.1.1 Transducer

A linear array transducer with 64 active elements is simulated both by Field II and Abersim. The pitch is 0.208 mm and the height is 4.5 mm for each element. The physical elevation focus is 20 mm. The electronic focus of the 64 active elements is set to 40 mm from the transducer surface. The data for the simulated transducer is acquired from an exist transducer - BK8804

(from BK Medical Aps, Herlev, Denmark). Its impulse response is measured as shown in Fig. 4.1 and then used in the simulation. A 2-cycle sine wave with the center frequency of $f_0 = 5$ MHz is used as the excitation.

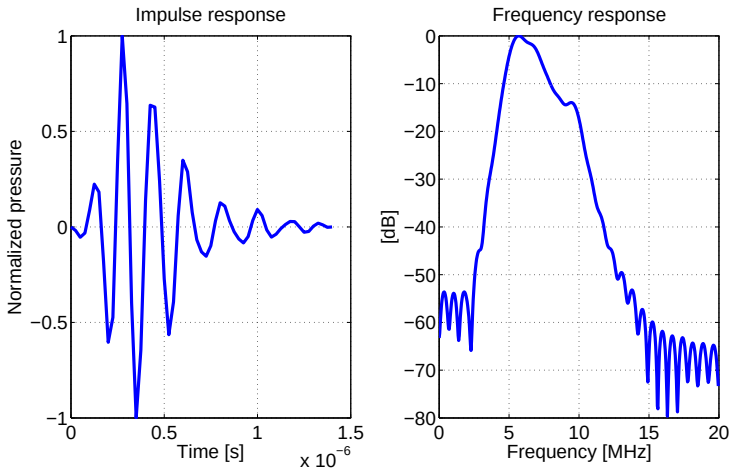

Figure 4.1: Impulse and frequency response of the transducer - The data was acquired from an exist transducer - BK8804, manufactured by BK Medical Aps, Herlev, Denmark.

4.1.2 Parameters of transmit medium and its non-linearity

Assuming that the simulation is in water at atmospheric pressure and the temperature is 20 degrees Celsius. The sound speed c_0 is 1482.3 m/s and the density ρ_0 is 1000 kg/m^3. The non-linearity coefficient β for water is 3.48 in this case. The amplitude of the initial acoustic pressure from the transducer is 50 kPa. The initial parameters presented in this section are used both in the Field II and Abersim simulations. The attenuation of water is very low and not included in the simulation.

4.1.3 Setup of Field II

The transducer is simulated in Field II by the function xdc_focused_array [49], where the parameters for each individual element, elevation and electronic foci can be set. The temporal sampling frequency (f_s) is 100 MHz. The acoustic source plane of the ASA is 1 mm from the transducer surface and calculated in Field II by the function calc_hp. The plane has 34×100 (y-x plane) points with spatial sampling

intervals of a half wavelength ($\lambda = c_0/f_0$, $\lambda/2 = 0.14823$ mm), which satisfies Nyquist-Shannon Sampling Theorem [50]. The whole area of the plane is 5×14.8 mm^2 a little bit bigger than the active aperture of the transducer, whose area is 4.5×13.312 mm^2 for the 64 elements.

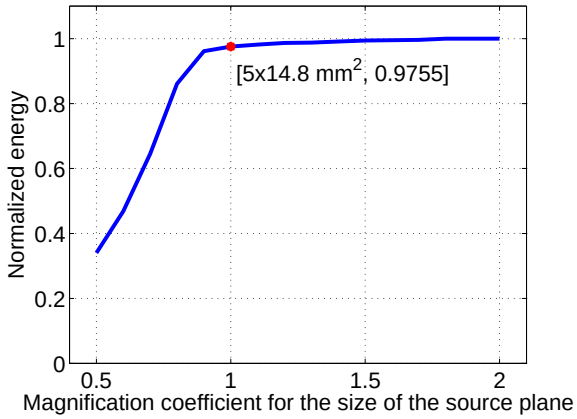

Figure 4.2: Energy of the source with different size - The figure shows how the energy in the source plane changes as a function of the source plane size. The energy is normalized to the largest calculated plane, which has twice length and width of the used source plane in the simulation. The red point shows the information of used source plane.

As described in the previous chapter, the ASA source plane should be large enough to cover all the acoustic waves propagating from the original source which is generated by Field II. Fig. 4.2 shows the normalized energy of the source with different size. The x-axis (horizontal) is the magnification coefficient of the size for the source plane, which represents the ratio of the length and width of the source to that of the used source (5×14.8) mm^2 in the simulation. The y-axis (vertical) is the energy contained in the plane with the corresponding size normalized to the twice length and width of the used source. The red point is the size of the source used in the simulation. The energy contained in the plane becomes almost unchanged after the red point, when the size of the plane is increased. The total energy using the size shown in the red point is 0.9755 of the energy of the twice length and width's plane. The acoustic energy can be calculated by Field II using the function `calc_hp`, where it is considered that the sum for the square of each amplitude of the pulse is proportional to the acoustic energy.

4.1.4 Setup of Abersim

The same transducer is simulated in Abersim. The function flags [23] in Abersim are [1, 1, 0, 0, 0, 0, 3]. The first two flags represent that diffraction and non-linearity are switched on. The next four flags are zeros, which denote lossless and homogeneous medium, non-annular transducer, and equidistant steps. The last flag is a history flag and "3" means that Abersim will store each pulse at each depth. Although it is likely to slow the simulation compared with using a history flag "0", which means no pulse is exported or stored on a disk except the final result at the end of the simulated depth. An experiment for simulating this transducer shows the speed using the history flag "0" is only increased by 1% compared to "3".

The step size between two nearby planes is 0.25 mm set by default by Abersim based on the imaging frequency according to the Earnshaw or Poisson solution [6]. Abersim simulates non-linear fields by numerically solving the Burgers equation, which results in a pulse with all harmonic components. A pulse inversion (PI) [1, 3, 4] technique is used to remove the odd harmonic (e.g. 1st, 3rd, 5th, etc.) components. This is made by sending an inverted excitation pulse at the second simulation and only even harmonic (e.g. 2nd, 4th, 6th, etc.) components are left by summing the results from two simulations. Then a bandpass filter is applied to obtain the second harmonic pulse. Likewise, the fundamental pulse can be attained by subtracting the results from two simulations. Thus, the even harmonic components are removed this time and the fundamental pulse is obtained by filtering out other odd harmonic (3rd, 5th, etc.) components. (See Appendix B for the figures in the process of getting the isolated fundamental and second harmonic components from the Abersim)

4.2 Results for emitted fields

The emitted field at the focal distance 40 mm from the transducer surface is shown in Fig. 4.3. The contour plots present the point spread functions of the fundamental and second harmonic fields along the lateral direction in the time domain at $y = 0$ (elevation). The envelope of the pulses in logarithmic scale, obtained by the Hilbert transform, are illustrated. There is 6 dB difference between each adjacent contours. The power at the focal depth for each spatial point along the lateral direction (x-axis) is calculated by summing the square of the pressure along the time-axis and divided by the time length.

This can be expressed by

$$P_{ower}(n_x) = \frac{1}{N_T} \sum_{n_t=0}^{N_T-1} p(n_x, n_t)^2, \tag{4.1}$$

where n_x and n_t are index numbers for the x-axis and time-axis, $P_{ower}(n_x)$ is the discrete power along the x-axis, and $p(n_x, n_t)$ is the discrete pressure along the x-axis and time-axis. N_T is the total number of $p(n_x, n_t)$ along time-axis, and denotes the time length of the pulse. The power is calculated for the fundamental and second harmonic fields using the ASA and Abersim as shown in Fig. 4.4.

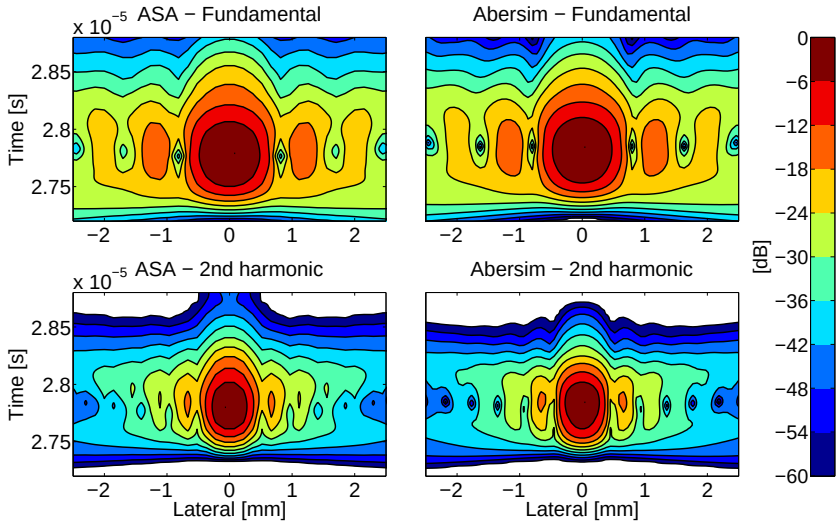

Figure 4.3: Point spread function of emitted field at the focal depth - The figure shows the emitted fields along the lateral direction at the focal depth 40 mm from the transducer surface calculated by the ASA based on Field II and by Abersim for the fundamental field on the top and for the second harmonic field on the bottom and 6 dB between two adjacent lines.

The fundamental and second harmonic pulses at the focal point simulated using ASA and Abersim are shown in Fig. 4.5. The ASA simulates the second harmonic pulse in one step, whereas Abersim needs hundreds of steps to reach the point, which is far from the source. Fig. 4.6 illustrates the comparison of the calculation time as a function of the image depth between using ASA and Abersim. This was made by Matlab 7.11.0(R2010b) using a computer with Q6600 2.4 GHz Intel(R) Core(TM)2 Quad CPU and 4 GB memory under the Ubuntu operating system. The pulse with all harmonic

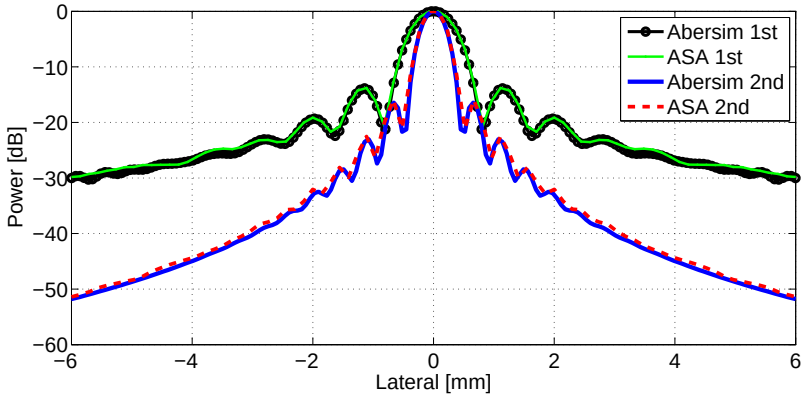

Figure 4.4: Power in lateral at the focal depth - The power is shown along the lateral direction for the fundamental and second harmonic fields calculated by the ASA based on Field II and by Abersim, respectively. In the legend, 1st means fundamental and 2nd means second harmonic.

components at the focal point, which is 40 mm from the transducer surface, has to be calculated after 160 iteration steps by the Abersim, which takes 840 minutes amounting to 14 hours. By using PI, the second harmonic pulse can be filtered out but the total time is doubled and up to 28 hours. The number of steps and the calculation complexity for the ASA is independent of image depth. Only one step is required, even if the point of calculated pulse is far from the transducer surface. For making the same simulation at the focal depth (40 mm) as Abersim, ASA takes 12 minutes. In this case, the speed is increased by a factor of 140.

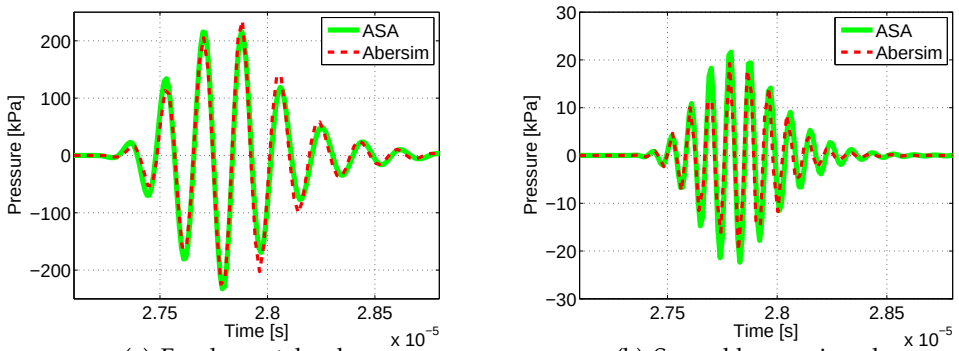

(a) Fundamental pulse (b) Second harmonic pulse

Figure 4.5: Fundamental and second harmonic simulation pulses - The fundamental and second harmonic pulses at the focal point are plotted. The pressure is shown in kilo Pascal.

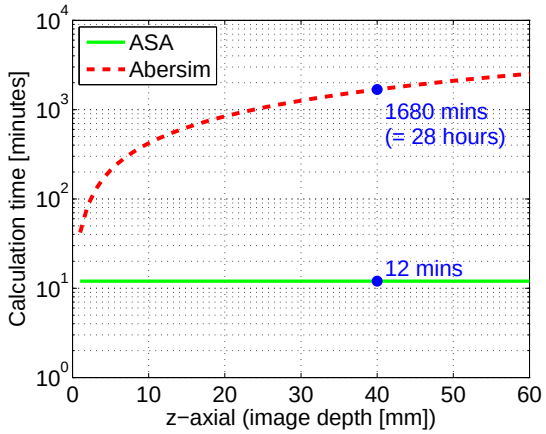

Figure 4.6: Calculation time of the ASA and Abersim - The figure shows the calculation time of the emitted field using the ASA and the Abersim as a function of image depth.

To further validate the results of the simulation from the ASA, comparisons between ASA and Abersim are made at depths of 30 mm and 60 mm from the transducer surface as shown in Figs. 4.7 and 4.8. Compared to the Abersim, the calculation time of the ASA is increased by a factor of 105 at 30 mm and 210 at 60 mm. Table 4.1 shows the full width (FW) at -6 dB and -12 dB for the fundamental and second harmonic pulses simulated by ASA and Abersim at depths of 30 mm, 40 mm, and 60 mm. The errors of FW at different depths are calculated as well by

$$\text{Error} = \frac{|\text{ASA} - \text{Abersim}|}{\text{Abersim}} \times 100\%, \tag{4.2}$$

ASA and Abersim in (4.2) denote their FWs.

4.3 Discussion

The ASA based on Field II can simulate pulsed non-linear ultrasound fields for array transducers with arbitrary geometry and short pulse excitation, that is much faster than current approaches. The results obtained at different depths without iteration steps are fairly comparable to those using Abersim. However, the ASA solution is made under the assumptions of weak nonlinearities. For the acoustic pressure with high amplitude or long propagation, the non-linear effect is much more obvious. First of all, all harmonic components should be taken into consideration. The exact equation for the total

Table 4.1: Comparison of the full width (FW) - The table shows the full width at -6 dB and -12 dB, and at depths of 30 mm, 40mm and 60 mm for ASA and Abersim. The error between ASA and Abersim is calculated by (4.2).

Depth = 30 mm		ASA	Abersim	Error
Fundamental	FW at -6 dB	2.97 mm	2.98 mm	0.6%
	FW at -12 dB	4.40 mm	4.41 mm	0.2%
2nd harmonic	FW at -6 dB	2.56 mm	2.62 mm	2.5%
	FW at -12 dB	3.37 mm	3.45 mm	2.4%
Depth = 40 mm		ASA	Abersim	Error
Fundamental	FW at -6 dB	0.97 mm	0.95 mm	1.7%
	FW at -12 dB	1.27 mm	1.26 mm	1.2%
2nd harmonic	FW at -6 dB	0.56 mm	0.55 mm	1.5%
	FW at -12 dB	0.77 mm	0.73 mm	6.4%
Depth = 60 mm		ASA	Abersim	Error
Fundamental	FW at -6 dB	6.06 mm	5.99 mm	1.1%
	FW at -12 dB	8.90 mm	8.82 mm	1.0%
2nd harmonic	FW at -6 dB	5.29 mm	5.21 mm	1.4%
	FW at -12 dB	7.01 mm	6.89 mm	1.6%

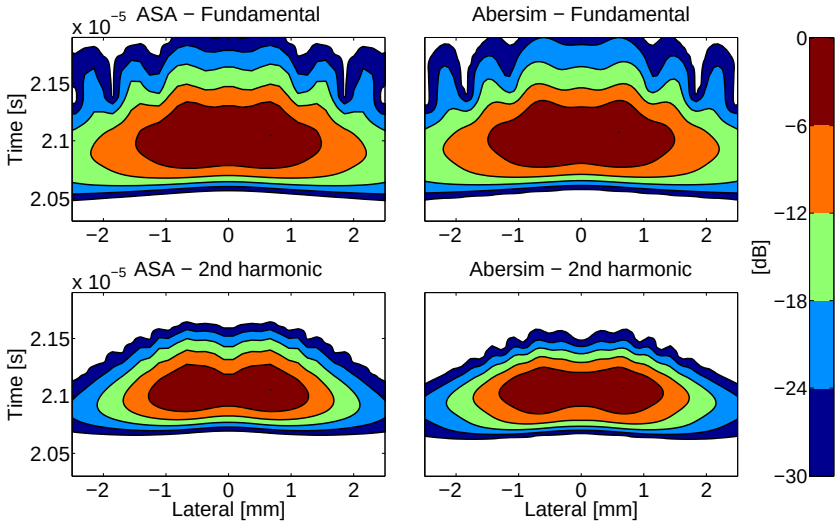

Figure 4.7: Point spread function of emitted field at 30 mm - The figure shows the emitted fields along the lateral direction at 30 mm from the transducer surface.

pressure should be $p = p_1 + p_2 + p_3 + ... + p_n$ instead of (2.30). Therefore, the calculated second harmonic pulse using the ASA in this chapter actually contained the energy of all of harmonic components ($p_2 + p_3 + ... + p_n$). This

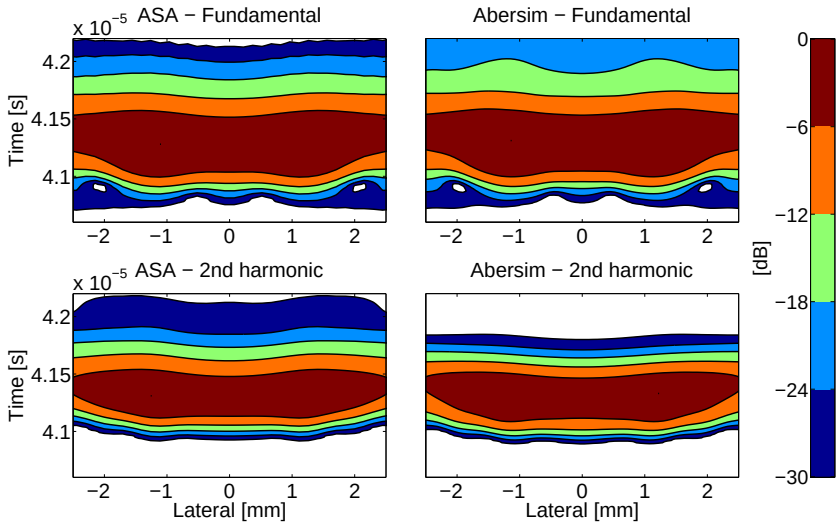

Figure 4.8: Point spread function of emitted field at 60 mm - The figure shows the emitted fields along the lateral direction at 60 mm from the transducer surface.

may be the reason why the absolute amplitude of pressure for the second harmonic pulse calculated using ASA is bigger than those using the Abersim as shown in Fig. 4.5b. The solutions to super harmonic components using the ASA are derived in Chapter 6.

The second assumption of the ASA from (2.31) in association with (2.30) also indicates that $p \approx p_1$ as p_1 is calculated using the linear ASA as given by (2.58). However, the ratio of p_2 to p_1 actually grows as the total pressure p grows. This will result in $p > p_1$ and p_1 should not be calculated linearly when the total pressure becomes high. In this simulation, the calculated peak amplitude of p_2 is approximately 20 dB lower than p_1 as shown in Fig. 4.5. Note that this is simulated under the assumption of $p_1 \gg p_2$ and the simulated results show that $p_1 \approx 10p_2$. Thus, the expected error will become larger and larger as the total pressure increases, that makes the ASA simulation constricted to a weak nonlinearity with relatively low-amplitude pressure.

However, the ultrasound pressure used in human tissue is usually not that large due to the attenuation. An example is shown in Fig. 4.9, which presents the peak amplitude of the acoustic pressure as a function of depth. The peak is recorded from the pulse at the center of the aperture ($x = 0, y = 0, z = [1 \sim 60]$ mm). The ultrasound field is simulated by Field II and created by the same linear array transducer, which has been used in the simulations for the ASA and Abersim. The average attenuation coefficient of biological materials

is used in the simulation, where $\alpha = 0.54$ dB/(MHz·cm) for the soft tissue. The figure shows that the maximum amplitude of a pressure field in water can be decreased to 300 kPa around in human tissue. The derated peak 300 kPa can also be assumed as the weak nonlinearity even though the peak in lossless medium is up to 1 MPa and it is still possible to make the simulation using the ASA in the human tissue.

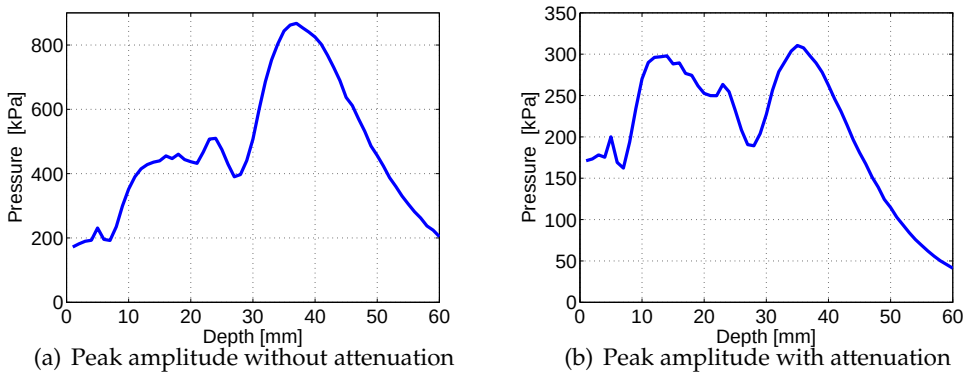

(a) Peak amplitude without attenuation (b) Peak amplitude with attenuation

Figure 4.9: Peak amplitude as a function of depth - The ultrasound field is created by the linear array transducer and the pressure is calculated by Field II. The left figure is the peak amplitude without attenuation and the right figure is the peak amplitude with attenuation (0.54 dB/(MHz·cm)).

CHAPTER

FIVE

Results from two Piston Transducers

This chapter presents the results obtained from two geometrically focused circular piston transducers. An under-water hydrophone measurement is made for these two piston transducers with diameters of 0.5 inch (12.7 mm) and 1 inch (25.4 mm). To further investigate the accuracy of the ASA, the measured results from the 0.5 inch and 1 inch transducers, are compared with the simulations of linear and non-linear ASA, respectively.

5.1 Simulation setup

The transducers are initialized by Field II, using the function xdc_concave in which the radius and focus distance can be set. The focus distance for 0.5 inch diameter ($d = 12.7$ mm) transducer is 62 mm and for 1 inch diameter ($d = 25.4$ mm) transducer is 118 mm. The ASA source as described in Chapter 3 should be close to the transducer surface for non-linear simulation. The size of it should be large enough to cover all acoustic waves propagating from the transducer and the interval between two adjacent spatial points should satisfy Nyquist-Shannon Sampling Theorem [50]. The ASA source is calculated by Field II, using the function calc_hp [49]. Table 5.1 shows the specific parameters for the ASA source used for simulating those two transducers.

Table 5.1: Parameters of the ASA source for simulating transducers

ASA source	Transducer (0.5 inch)	Transducer (1 inch)
Distance to transducer	12 mm	5 mm
Size	18.9×18.9 mm^2	30.5×30.5 mm^2
Points	128×128	412×412
Spatial interval	0.148 mm	0.074 mm

5.2 Measurement setup

The measurement is set up as shown in Fig. 5.1. A PVDF (polyvinylidene fluoride) ultrasonic hydrophone probe (MH28-5 made by Force Technology Aps, Denmark) is mounted in the focal plane of the transducers. It moves in the x-axis (lateral direction) and is controlled by the xyz-system. The transducer is fixed and excited by the waveform generator, which has a trigger pulse to an oscilloscope and synchronized with the excitation of the transducer. This makes the transducer emission and the oscilloscope data recording start at the same time. The maximum output voltage of the waveform generator for the transducer is 10 volts.

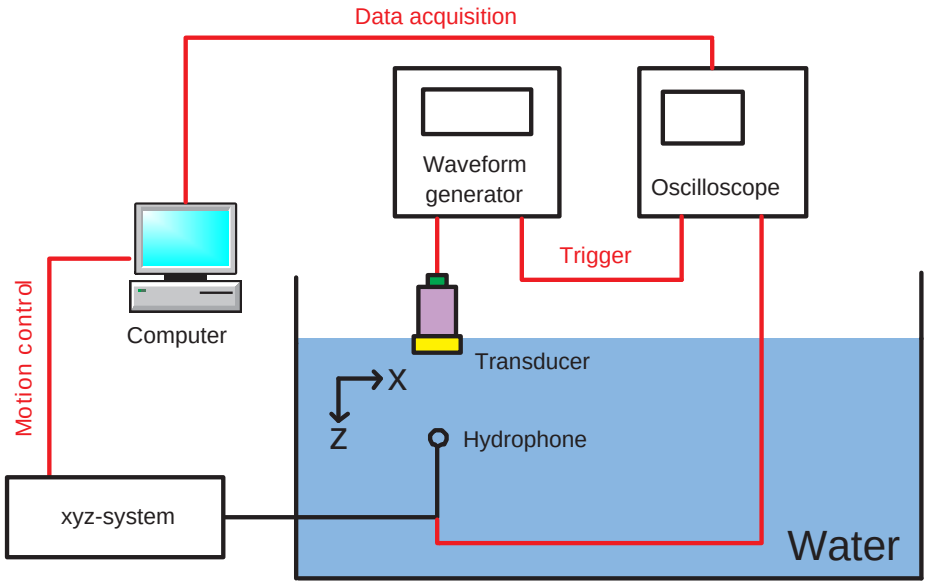

Figure 5.1: Schematic view of the water-tank hydrophone measurement

For each point in a fixed position, one acoustic pulse with a time line can be obtained. By moving the hydrophone along the lateral direction and mea-

suring the pulses at different position, the emitted field at the focal plane is acquired and stored in the oscilloscope. All these measurement activities can be controlled by a computer with Matlab scripts through GPIB (general purpose interface bus) and RS232 interface connections.

5.3 Results from 0.5 inch diameter transducer

The focused single element Panametrics ultrasonic transducer M309 is used for the transmission. The transducer has a diameter of 0.5 inch (12.7 mm) and its geometrical focus distance is 62 mm. The center frequency is 5 MHz and a 2-cycle sine wave is used in the measurement as the excitation. The signals generated by such a small transducer with 10 volts as the peak of the excitation are quite weak and not able to create non-linear effect. Therefore, the pure linear results will be presented for this transducer and compared to the ASA simulation. Fig. 5.2 shows the results calculated by linear pulsed ASA and Field II. The results are simulated at the focal plane, which is 62 mm from the transducer surface. The positions of these four pulses are shown in Fig. 5.3. It can be seen that both pulsed ASA and Field II create a fairly comparable in phase waves.

The point spread functions at the focal distance along the lateral direction for the ASA simulation and measurements are presented in Fig. 5.4. When the ASA calculates the pulse at the simulated plane, the accuracy of the sound speed becomes an issue, since the time line for the ASA calculated pulse is very dependent of the true sound speed in water for the measurement according to (2.58). Assume that the sound speed in water is 1480 m/s according to the temperature during the measurements. However, it will be very difficult to know an exact value of the real sound speed in water during each measurement. Even a half meter per second error of the sound speed can cause a shift of the pulses calculated by the ASA compared to the measured pulse. To find the correct sound speed, the time lag Δt between the pulse calculated by the ASA using the assumed sound speed 1480 m/s and the measured pulse can be expressed as

$$\Delta t = \frac{z_1}{c_a} - \frac{z_1}{c_r}, \tag{5.1}$$

where $z_1 = 62$ mm is the distance from the transducer surface to the measured point. c_a is the assumed sound speed 1480 m/s used in the ASA simulation, and c_r is the real sound speed during measurements and is the unknown variable in the equation. The time lag Δt can be found by apply-

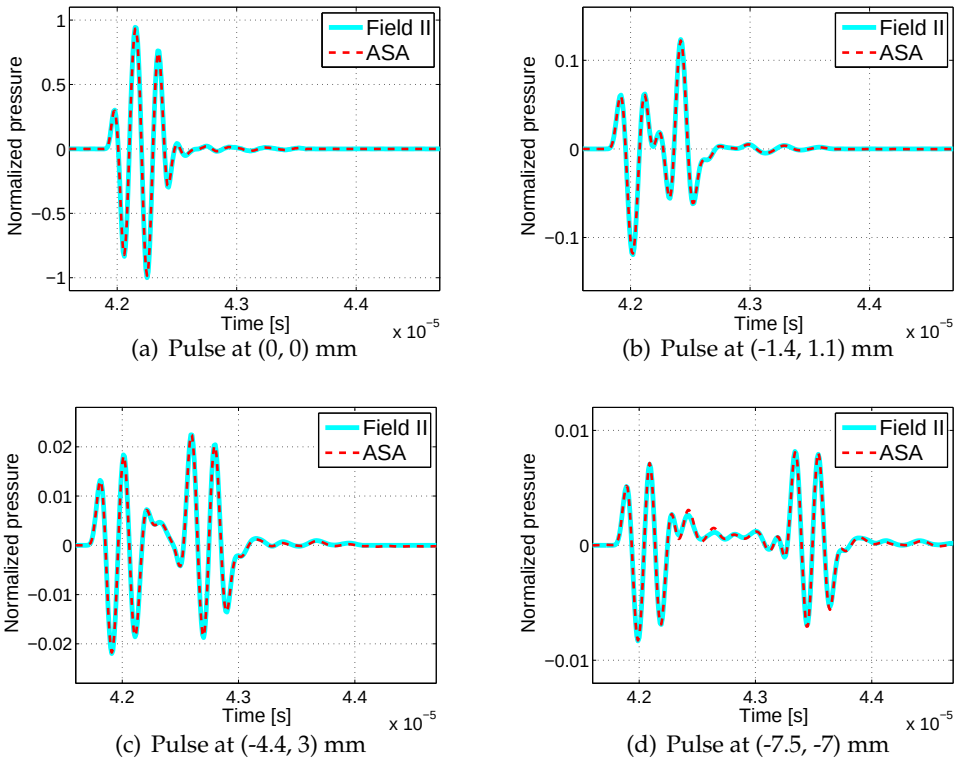

Figure 5.2: Simulated pulses by linear ASA - The figure shows four pulses simulated by ASA and Field II. The specific positions of these four pulses can be found in Fig. 5.3.

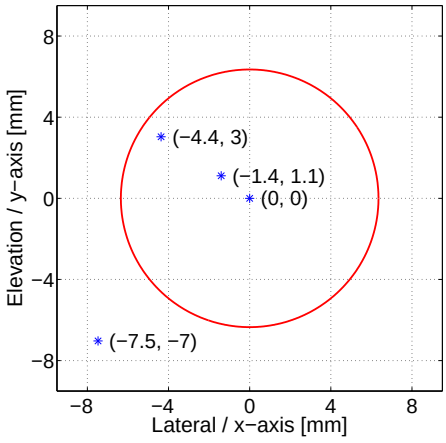

Figure 5.3: Positions of the four pulses - The figures shows the positions of the four pulses as shown in Fig. 5.2. All simulated points are at the focal plane, which is 62 mm from the transducer surface. The red circle denotes the size of the transducer.

ing the cross-correlation function to these calculated and measured pulses. By solving (5.1), c_r is obtained and reused in the ASA simulation. Thus, pulses between the ASA simulation and measurements are attained in phase as shown in Fig. 5.5, which is the pulses at the focal point. In this way, the sound speed is determined to be 1495.7 m/s.

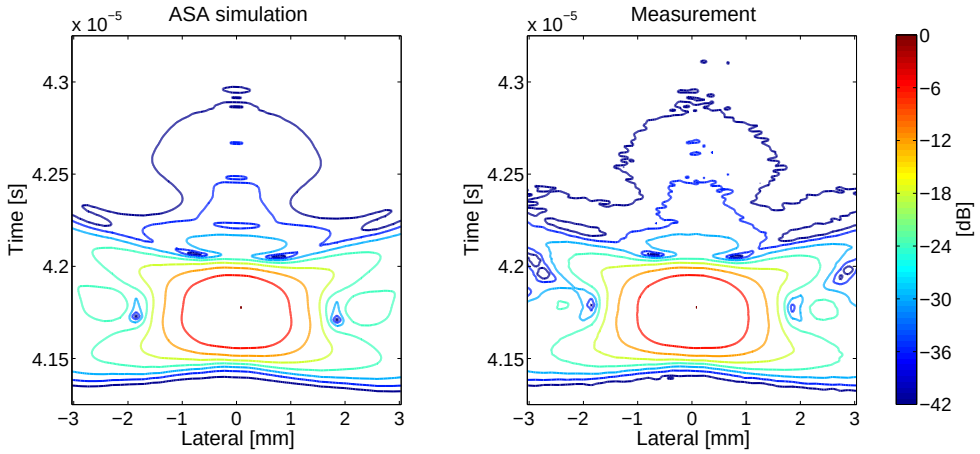

Figure 5.4: Point spread functions at the focal distance - The figures shows the point spread functions for the ASA simulation and hydrophone measurements. These are simulated and measured along lateral direction (x-axis), at the center of the transducer in elevation direction ($y = 0$) and at the focal distance ($z = 62$ mm).

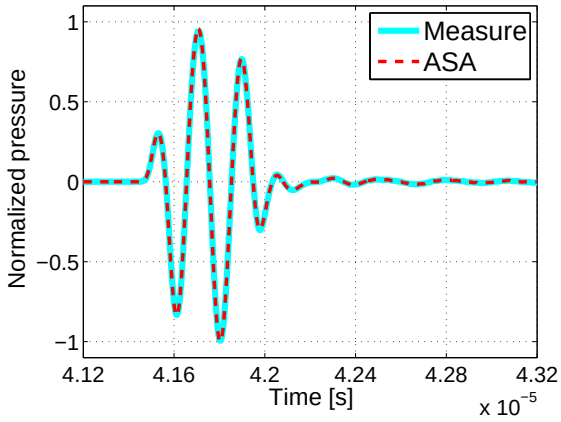

Figure 5.5: Pulses simulated and measured at the focal point - These are the time pulses at the focal point ($x = 0, y = 0, z = 62$ mm) simulated by ASA and measured under water. The measured time line is recorded by the oscilloscope. The simulated time line is corrected by (5.1). The sound speed used in the simulation is 1495.7 m/s.

5.4 Results from 1 inch diameter transducer

The focused single element Panametrics ultrasonic transducer V307 is used for the transmission. The transducer has a diameter of 1 inch (25.4 mm) and its geometrical focus distance is 118 mm. The center frequency is 5 MHz and a 6-cycle sine wave is used in the measurement as the excitation, which has more cycles than before and results in a lower bandwidth signal. This is for comparing with the simulation since the monochromatic field for the second harmonic component will be calculated by the ASA in this section. The results for the fundamental and second harmonic components along the lateral direction (x-axis) at the focal depth ($y = 0, z = 118$ mm) are shown in Fig 5.6, which presents the monochromatic field. One fixed temporal frequency component (5 MHz) is used in the ASA source. The second harmonic component at 10 MHz is calculated after propagation using the ASA. The measured fundamental and second harmonic components can be obtained by applying the temporal Fourier transform to the measured time pulses and then the frequency component can be extracted from it.

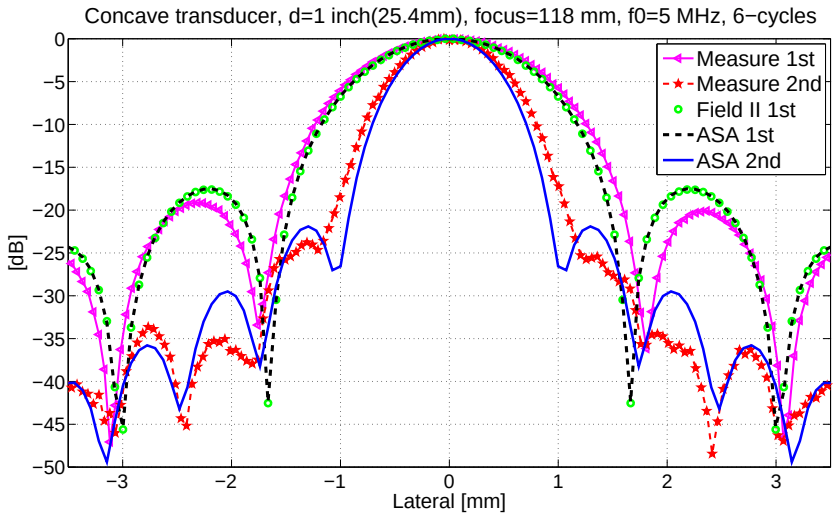

Figure 5.6: Comparison between measurements and simulations - These are calculated and measured along the lateral direction (x-axis) at the focal distance ($y = 0, z = 118$ mm from the transducer surface). The results obtained from each method or measurement for the fundamental or second harmonic components are normalized to themselves, which means the absolute difference between the fundamental and second harmonic components is not shown in the figure. In the legend, 1st means fundamental frequency component at 5 MHz and 2nd means second harmonic component at 10 MHz.

The quantitative comparisons are made by the RMS (root mean square) errors

$$\text{RMS-error}(f) = \sqrt{\frac{\sum_{i_x=0}^{N=93} \left[P_{\text{c}}(i_x, f) - P_{\text{ref}}(i_x, f)\right]^2}{\sum_{i_x=0}^{N=93} P_{\text{ref}}(i_x, f)^2}} \times 100\%, \tag{5.2}$$

where $P_{\text{c}}(i_x, f)$ is the discrete form of the pressure simulated by the ASA or Field II at the focal plane ($y = 0$, $z = 118$ mm) and a function distributed along x-axis (lateral direction) where i_x is from 0 to 93 corresponding to $(-3.5 \sim 3.5)$ mm, and f can be 5 MHz or 10 MHz in this case. $P_{\text{ref}}(i_x, f)$ is the reference pressure measured in the water tank or simulated by the Field II program at the same location for the same frequency components. The RMS errors are shown in Table 5.2.

Table 5.2: RMS errors between ASA, Field II and measurements

	$P_{\text{c}}(i_x, f)$	$P_{\text{ref}}(i_x, f)$	Frequency	RMS-error(f)
1	Field II	Measure	Fundamental 5 MHz	7.39%
2	ASA	Field II	Fundamental 5 MHz	0.67%
3	ASA	Measure	Fundamental 5 MHz	7.19%
4	ASA	Measure	Second harmonic 10 MHz	10.3%

Comparison 2 in Table 5.2 reveals that the two simulation methods give very similar results. By use of the ASA based on the Field II program, the generation of second harmonic component during the acoustic propagation can be studied in the simulation.

CHAPTER

SIX

Super Harmonic Calculations using the ASA

The second harmonic ultrasound field has been successfully simulated by implementing the ASA, which may be extended to calculate the third or even higher harmonic fields. This chapter is dedicated to deriving an expression of the third harmonic fields using the ASA based on the theory described in Chapter 2.

6.1 Equations of super harmonic fields

The ASA solution to the second harmonic fields was previously obtained based on two assumptions as expressed in (2.30) and (2.31). To calculate the third harmonic component, the total sound pressure after propagation should be assumed as the sum of all of the harmonic components so that (2.30) will be rewritten as

$$p = p_1 + p_2 + p_3 + ... + p_n, \tag{6.1}$$

where p_n is the nth harmonic pressure. Similarly, substituting (2.32) and (6.1) into the lossless Westervelt equation (2.28) leads to

$$\sum_{n=1}^{+\infty}(\nabla^2 + n^2k^2)P_n e^{-jn\omega t} = -\frac{\beta}{2\rho_0 c_0^4}\frac{\partial}{\partial t^2}\sum_{n=1}^{+\infty}(P_n e^{-jn\omega t})^2, \tag{6.2}$$

where n is an integer number starts from 1. This equation contains all of the harmonic components, which are generated during the non-linear propaga-

tion. It can be expanded by

$$\begin{aligned}
(\nabla^2 + k^2)P_1 e^{-j\omega t} &= -\frac{\beta}{2\rho_0 c_0^4}\frac{\partial}{\partial t^2}\Big(P_1 e^{-j\omega t} + P_2 e^{-2j\omega t} \\
&+ \qquad\qquad + P_3 e^{-3j\omega t} + P_4 e^{-4j\omega t} \\
(\nabla^2 + 4k^2)P_2 e^{-2j\omega t} &\qquad\qquad + P_5 e^{-5j\omega t} \cdots\Big)^2 \\
&+ \\
(\nabla^2 + 9k^2)P_3 e^{-3j\omega t} & \\
&+ \\
(\nabla^2 + 16k^2)P_4 e^{-4j\omega t} & \\
&+ \\
(\nabla^2 + 25k^2)P_5 e^{-5j\omega t} & \\
\vdots &
\end{aligned} \tag{6.3}$$

The right hand side of (6.3) can be further derived and expressed by

$$\begin{aligned}
(\nabla^2 + k^2)P_1 e^{-j\omega t} &= -\frac{\beta}{2\rho_0 c_0^4}\frac{\partial}{\partial t^2}\Big[P_1^2 e^{-2j\omega t} + 2P_1 P_2 e^{-3j\omega t} \\
&+ \qquad\qquad + (2P_1 P_3 + P_2^2)e^{-4j\omega t} \\
(\nabla^2 + 4k^2)P_2 e^{-2j\omega t} &\qquad\qquad + (2P_1 P_4 + 2P_2 P_3)e^{-5j\omega t} \cdots\Big] \\
&+ \\
(\nabla^2 + 9k^2)P_3 e^{-3j\omega t} & \\
&+ \\
(\nabla^2 + 16k^2)P_4 e^{-4j\omega t} & \\
&+ \\
(\nabla^2 + 25k^2)P_5 e^{-5j\omega t} & \\
\vdots &
\end{aligned} \tag{6.4}$$

The right hand side of (6.4) can be further derived as

$$\begin{aligned}
R_{(6.4)} &= \frac{\beta k^2}{\rho_0 c_0^2}\Big[2P_1^2 e^{-2j\omega t} + 9P_1 P_2 e^{-3j\omega t} \\
&\quad +8(2P_1 P_3 + P_2^2)e^{-4j\omega t} + 25(P_1 P_4 + P_2 P_3)e^{-5j\omega t} \cdots\Big]
\end{aligned} \tag{6.5}$$

Substituting (6.5) into (6.4) and, thus, making both the left and right hand sides of (6.4) divided by $e^{-j\omega t}$ gives

$$\begin{aligned}
(\nabla^2 + k^2)P_1 &= \frac{\beta k^2}{\rho_0 c_0^2}\Big[2P_1^2 e^{-j\omega t} + 9P_1 P_2 e^{-2j\omega t} \\
+ & \quad +8(2P_1 P_3 + P_2^2)e^{-3j\omega t} \\
(\nabla^2 + 4k^2)P_2 e^{-j\omega t} & \quad +25(P_1 P_4 + P_2 P_3)e^{-4j\omega t} \cdots \Big] \\
+ & \\
(\nabla^2 + 9k^2)P_3 e^{-2j\omega t} & \\
+ & \\
(\nabla^2 + 16k^2)P_4 e^{-3j\omega t} & \\
+ & \\
(\nabla^2 + 25k^2)P_5 e^{-4j\omega t} & \\
\vdots &
\end{aligned} \tag{6.6}$$

The first term of the left hand side in (6.6) is not a function of time t, which gives

$$(\nabla^2 + k^2)P_1 = 0. \tag{6.7}$$

Substituting (6.7) into (6.6) and making it divided by $e^{-j\omega t}$ again yields

$$\begin{aligned}
(\nabla^2 + 4k^2)P_2 &= \frac{\beta k^2}{\rho_0 c_0^2}\Big[2P_1^2 + 9P_1 P_2 e^{-j\omega t} \\
+ & \quad +8(2P_1 P_3 + P_2^2)e^{-2j\omega t} \\
(\nabla^2 + 9k^2)P_3 e^{-j\omega t} & \quad +25(P_1 P_4 + P_2 P_3)e^{-3j\omega t} \cdots \Big] \\
+ & \\
(\nabla^2 + 16k^2)P_4 e^{-2j\omega t} & \\
+ & \\
(\nabla^2 + 25k^2)P_5 e^{-3j\omega t} & \\
\vdots &
\end{aligned} \tag{6.8}$$

This will lead to the expression for the second harmonic component, which is written by

$$(\nabla^2 + 4k^2)P_2 = \frac{2\beta k^2}{\rho_0 c_0^2}P_1^2. \tag{6.9}$$

Similarly, the third and higher harmonic components can be derived and expressed as

$$(\nabla^2 + 9k^2)P_3 = \frac{9\beta k^2}{\rho_0 c_0^2} P_1 P_2. \tag{6.10}$$

$$(\nabla^2 + 16k^2)P_4 = \frac{8\beta k^2}{\rho_0 c_0^2}(2P_1 P_3 + P_2^2). \tag{6.11}$$

$$(\nabla^2 + 25k^2)P_5 = \frac{25\beta k^2}{\rho_0 c_0^2}(P_1 P_4 + P_2 P_3). \tag{6.12}$$

These are the equations for modeling the 3rd, 4th and 5th harmonic components. The higher (more than 5th) harmonic component can also be derived in this way, though it is not presented in this dissertation.

6.2 Solution to the super harmonic components using the ASA

The higher harmonic components can also be solved using the ASA by the similar equation derivations as described in Chapter 2. This section will present a detailed derivation of the ASA solution to (6.10) for the third harmonic component. The derivation from (2.37) to (2.51) in Chapter 2 can be transplanted to solve the third harmonic component for (6.10). Referred to (2.51), (6.10) can be derived as

$$\left(\frac{d^2}{dz^2} + k_{z3}^2\right)\hat{P}_3(k_x, k_y, z_1) = \frac{9\beta k^2}{4\pi^2 \rho_0 c_0^2} M'(k_x, k_y, z_1), \tag{6.13}$$

where

$$M'(k_x, k_y, z_1) = \iint \hat{P}_2(k'_x, k'_y, z_0) \times \hat{P}_1(k_x - k'_x, k_y - k'_y, z_0) dk'_x dk'_y, \tag{6.14}$$

$$k_{z3} = \sqrt{9k^2 - k_x^2 - k_y^2}, \tag{6.15}$$

$$k''_z = \sqrt{k^2 - (k_x - k'_x)^2 - (k_y - k'_y)^2}. \tag{6.16}$$

The solution to (6.13), which is an ordinary differential equation with an inhomogeneous integral term, can be found as referred to the similar derivations for the second harmonic component in Appendix A.3. Similarly as (A.46),

$\hat{P}_3(k_x, k_y, z)$ at $z = z_1$ can be written as

$$\begin{aligned}\hat{P}_3(k_x, k_y, z_1) &= A' e^{-jk_{z3}z_1} + \eta' e^{-jk_{z3}z_1} \int_{z_0}^{z_1} e^{j2k_{z3}z_1'} \int_{z_0}^{z_1'} e^{-jk_{z3}z} \iint \\ &\quad \times \hat{P}_2(k_x', k_y', z_1) \hat{P}_1(k_x - k_x', k_y - k_y', z_1) dk_x' dk_y' dz dz_1',\end{aligned} \tag{6.17}$$

where

$$\eta' = \frac{9\beta k^2}{4\pi^2 \rho_0 c_0^2}. \tag{6.18}$$

Substituting (2.48) and (2.56), which are the expressions of ASA used for calculating the fundamental and second harmonic components, into (6.17) leads to

$$\begin{aligned}\hat{P}_3 &= A' e^{-jk_{z3}z_1} + \eta'\eta \iiiint e^{-jk_{z3}z_1} \int_{z_0}^{z_1} e^{j2k_{z3}z_1'} \int_{z_0}^{z_1'} e^{-jk_{z3}z} \hat{P}_0(k_x'', k_y'', z_0) \\ &\quad \times \frac{e^{-j(z-z_0)(\bar{k}_z' + \bar{k}_z'')} - e^{-j(z-z_0)k_{z2}'}}{k_{z2}'^2 - (\bar{k}_z' + \bar{k}_z'')^2} \hat{P}_0(k_x' - k_x'', k_y' - k_y'', z_0) \\ &\quad \times e^{-j(z-z_0)k_z''} \hat{P}_0(k_x - k_x', k_y - k_y', z_0) dz dz_1' dk_x' dk_y' dk_x'' dk_y'',\end{aligned} \tag{6.19}$$

where η has been described in (A.36) and

$$k_{z2}' = \sqrt{4k^2 - k_x'^2 - k_y'^2}, \tag{6.20}$$

$$\bar{k}_z' = \sqrt{k^2 - (k_x'')^2 - (k_y'')^2}, \tag{6.21}$$

$$\bar{k}_z'' = \sqrt{k^2 - (k_x' - k_x'')^2 - (k_y' - k_y'')^2}. \tag{6.22}$$

For convenience, the multiplication of 3 $\hat{P}_0$ in (6.19) is replaced by

$$\alpha = \hat{P}_0(k_x'', k_y'', z_0) \times \hat{P}_0(k_x' - k_x'', k_y' - k_y'', z_0) \times \hat{P}_0(k_x - k_x', k_y - k_y', z_0). \tag{6.23}$$

$\hat{P}_3(k_x, k_y, z_1)$ can be further simplified to

$$\begin{aligned}\hat{P}_3 &= A' e^{-jk_{z3}z_1} + \eta'\eta \iiiint \alpha e^{-jk_{z3}(z_1 - z_0)} \int_{z_0}^{z_1} e^{j2k_{z3}(z_1' - z_0)} \\ &\quad \times \int_{z_0}^{z_1'} \frac{e^{-j(z-z_0)(\bar{k}_z' + \bar{k}_z'' + k_z'' + k_{z3})} - e^{-j(z-z_0)(k_{z2}' + k_z'' + k_{z3})}}{k_{z2}^2 - (\bar{k}_z' + \bar{k}_z'')^2} \\ &\quad \times dz dz_1' dk_x' dk_y' dk_x'' dk_y''.\end{aligned} \tag{6.24}$$

After simplifying two integrals with respect to z, $\hat{P}_3(k_x, k_y, z_1)$ becomes

$$\begin{aligned}\hat{P}_3 &= A'e^{-jk_{z3}z_1} + \eta'\eta \iiiint \Big[\frac{e^{-jk_{z3}(z_1-z_0)}}{2k_{z3}(\bar{k}'_z+\bar{k}''_z+k''_z+k_{z3})[k'^2_{z2}-(\bar{k}'_z+\bar{k}''_z)^2]} \\ &+\frac{e^{-j(z_1-z_0)(\bar{k}'_z+\bar{k}''_z+k''_z)}-e^{-jk_{z3}(z_1-z_0)}}{(\bar{k}'_z+\bar{k}''_z+k''_z+k_{z3})(\bar{k}'_z+\bar{k}''_z+k''_z-k_{z3})[k'^2_{z2}-(\bar{k}'_z+\bar{k}''_z)^2]} \\ &-\frac{e^{-j(z_1-z_0)(k'_{z2}+k''_z)}-e^{-jk_{z3}(z_1-z_0)}}{(k'_{z2}+k''_z+k_{z3})(k'_{z2}+k''_z-k_{z3})[k'^2_{z2}-(\bar{k}'_z+\bar{k}''_z)^2]} \\ &-\frac{e^{-jk_{z3}(z_1-z_0)}}{2k_{z3}(k'_{z2}+k''_z+k_{z3})[k'^2_{z2}-(\bar{k}'_z+\bar{k}''_z)^2]}\Big]\alpha dk'_x dk'_y dk''_x dk''_y. \end{aligned} \tag{6.25}$$

It is assumed that the acoustic source does not generate non-linear components. This boundary condition can be expressed by

$$\hat{P}_3(k_x, k_y, z_0) = 0. \tag{6.26}$$

Substituting $z_1 = z_0$ into (6.25), thus yields

$$\begin{aligned}\hat{P}_3 &= A'e^{-jk_{z3}z_0} + \eta'\eta \iiiint \Big[\frac{1}{2k_{z3}(\bar{k}'_z+\bar{k}''_z+k''_z+k_{z3})[k'^2_{z2}-(\bar{k}'_z+\bar{k}''_z)^2]} \\ &-\frac{1}{2k_{z3}(k'_{z2}+k''_z+k_{z3})[k'^2_{z2}-(\bar{k}'_z+\bar{k}''_z)^2]}\Big]\alpha dk'_x dk'_y dk''_x dk''_y. \end{aligned} \tag{6.27}$$

Using (6.26), (6.27) becomes

$$\begin{aligned}A' &= -\eta'\eta e^{jk_{z3}z_0} \iiiint \Big[\frac{1}{2k_{z3}(\bar{k}'_z+\bar{k}''_z+k''_z+k_{z3})[k'^2_{z2}-(\bar{k}'_z+\bar{k}''_z)^2]} \\ &-\frac{1}{2k_{z3}(k'_{z2}+k''_z+k_{z3})[k'^2_{z2}-(\bar{k}'_z+\bar{k}''_z)^2]}\Big]\alpha dk'_x dk'_y dk''_x dk''_y. \end{aligned} \tag{6.28}$$

Substituting (A.36), (6.18), (6.23) and (6.28) into (6.25) results in

$$\begin{aligned}\hat{P}_3(k_x, k_y, z_1) &= \frac{9\beta^2 k^4}{8\pi^4\rho_0^2 c_0^4} \iiiint \Big[\frac{e^{-j(z_1-z_0)(k'_{z2}+k''_z)}-e^{-j(z_1-z_0)k_{z3}}}{[k^2_{z3}-(k'_{z2}+k''_z)^2][k'^2_{z2}-(\bar{k}'_z+\bar{k}''_z)^2]} \\ &-\frac{e^{-j(z_1-z_0)(\bar{k}'_z+\bar{k}''_z+k''_z)}-e^{-j(z_1-z_0)k_{z3}}}{[k^2_{z3}-(\bar{k}'_z+\bar{k}''_z+k''_z)^2][k'^2_{z2}-(\bar{k}'_z+\bar{k}''_z)^2]}\Big] \\ &\times\hat{P}_0(k''_x, k''_y, z_0)\hat{P}_0(k'_x-k''_x, k'_y-k''_y, z_0) \\ &\times\hat{P}_0(k_x-k'_x, k_y-k'_y, z_0)dk'_x dk'_y dk''_x dk''_y. \end{aligned} \tag{6.29}$$

This is the final solution which is derived by the ASA for calculating the third harmonic component. Note that this is the solution under the condition of $k^2 > (k''_x)^2 + (k''_y)^2$, $4k^2 > (k'_x)^2 + (k'_y)^2$, $k^2 > (k_x - k'_x)^2 + (k_y - k'_y)^2$,

$k^2 > (k'_x - k''_x)^2 + (k'_y - k''_y)^2$ and $9k^2 > k_x^2 + k_y^2$. The condition includes five inequalities with each including two possibilities. This will give $2^5 = 32$ equations under different conditions. To calculate pulsed ultrasound fields, the temporal frequency f will be the fourth variables of $\hat{P}_3$ in (6.29). This is very similar as the extension of the second harmonic component from the monochromatic to pulsed fields as described in Chapter 2. The inverse Fourier transform (1D in time and 2D in space) is given by

$$p_3(x, y, z_1, t) = \frac{1}{(2\pi)^2} \iiint_{-\infty}^{\infty} \hat{P}_3(k_x, k_y, z_1, 3f) e^{j(k_x x + k_y y + 2\pi f t)} dk_x dk_y df, \quad (6.30)$$

where $p_3(x, y, z_1, t)$ is the third harmonic pressure in the spatial time domain, $\hat{P}_3(k_x, k_y, z_1, 3f)$ is calculated by (6.29) and $\hat{P}_0$ in (6.29) can be obtained by (2.63). Note that there will be 64 solution equations finally after adding the conditions for the temporal frequency f.

6.3 Discussion

The implementing equation of the third harmonic component for pulsed ultrasound fields using the ASA has been derived in this chapter. Similarly as the second and third harmonic components derived from (6.9) and (6.10), the higher harmonic components can also be derived and obtained using (6.11), (6.12) and so forth. To calculate P_2, P_1 has to be a known variable as expressed in (6.9). Likewise, P_1 and P_2 should be known variables for calculating P_3 as expressed in (6.10). In this way, the implementing equations for all harmonic components can theoretically be found one by one as long as P_1 is a known variable. For weak nonlinearity, the fundamental component P_1 is calculated with the assumption of linear propagation using the ASA as expressed in (2.58). However, the amplitude of the fundamental component P_1 will be depressed by its corresponding higher harmonic components through the non-linear propagation. As described in Chapter 4, Section 4.3, the linearly calculated fundamental component P_1 will become larger than it should be used in the calculation of second or higher harmonic components. That is the reason why the ASA has the limitation for simulating the strong nonlinearity.

CHAPTER

SEVEN

Preliminary Study of Dual-Stage Harmonic Imaging

Non-linear ultrasound imaging may be combined with other imaging methods to further improve the resolution. The conventional harmonic imaging uses a fixed transmit focus and dynamic receive focus (DRF). Synthetic aperture imaging is a well-know ultrasound imaging method, where the dynamic focus can be achieved both in transmit and receive. The synthetic aperture harmonic imaging has been introduced by Bae et al [51] in 2008. In the conventional synthetic aperture imaging, a single element is used for emissions to simulate a spherical wave. The major drawback is that the transmitting energy for a single element is too low, so that the harmonic signals become much lower. Although there can be a multi-element emission used to enhance the transmitting energy and simulate a virtual focal point behind or in front of the transducer, there is still lots of storage required for saving the data for each low resolution image, when using the conventional synthetic aperture imaging.

Synthetic aperture sequential beamforming (SASB) is a novel technique and also called dual-stage beamforming, which has been researched and developed by Kortbek et al [52–54] in 2007. The advantage of SASB is that the lateral resolution is improved independently of image depth compared to the conventional ultrasound imaging using the DRF. SASB can be thought of as a two-stage procedure. The first stage is to obtain a set of conventional B-mode image lines with the same fixed transmit and receive focal point. Then, the image is created by synthetic aperture imaging using the B-mode image lines in the second stage. In this way, not only is dynamic focusing in both transmit and receive achieved, but the memory requirements are also reduced, since each low resolution image is only stored in one B-mode line. In the first stage

of SASB, a number of elements are used for a fixed focus transmission. Thus, a high penetration and SNR for harmonic imaging can be carried out through this assumption.

The purpose of this study is to investigate harmonic imaging using the dual-stage synthetic aperture sequential beamforming. The measured results using different imaging methods are illustrated, compared and concluded as follows. A discussion with future developments is given at the end of this chapter.

7.1 Measured results

The investigation is made by an experimental Synthetic Aperture Real-time Ultrasound Scanner (SARUS) [55]. A linear array transducer (BK8804, from BK Medical Aps) is used to transmit and receive data from a wire phantom in water. The transducer specifications are described in Chapter 4 and its impulse and frequency responses can be found in Fig. 4.1. There are four wires as point targets at the image depth of 22.5 mm, 47.5 mm, 72.5 mm and 97.5 mm, respectively. Three different experiments are made using three different transmit foci, which are 10 mm, 25 mm and 50 mm from the transducer surface, respectively. A two-cycle sine wave with a center frequency of 5 MHz is used as the excitation.

Four imaging methods which are dynamic receive focus imaging (DRFI), dynamic receive focus harmonic imaging (DRFHI), synthetic aperture sequential beamforming imaging (SASBI) and synthetic aperture sequential beamforming harmonic imaging (SASBHI), have been performed to investigate the resolution of ultrasound images. The harmonic imaging is implemented using a pulse inversion technique. The received RF lines obtained from SARUS are post-processed by a Beamformation Toolbox [56, 57] to achieve the dynamic receive focus and the synthetic aperture sequential beamforming.

The images for the same wire phantom using the different methods are shown in Fig. 7.1. The FWHM (full width at half maximum (-6 dB)) and FWOTM (full width at one tenth maximum (-20 dB)) along the lateral direction are calculated for each point in each image and shown in Tables 7.1 and 7.2. The comparison among those four imaging methods should be made using the optimized ultrasound image of each method. There are three measurements with different transmit focuses were made for each method. The FWHM and FWOTH for those four measured points and the average resolution as a function of depth should be evaluated for different transmit

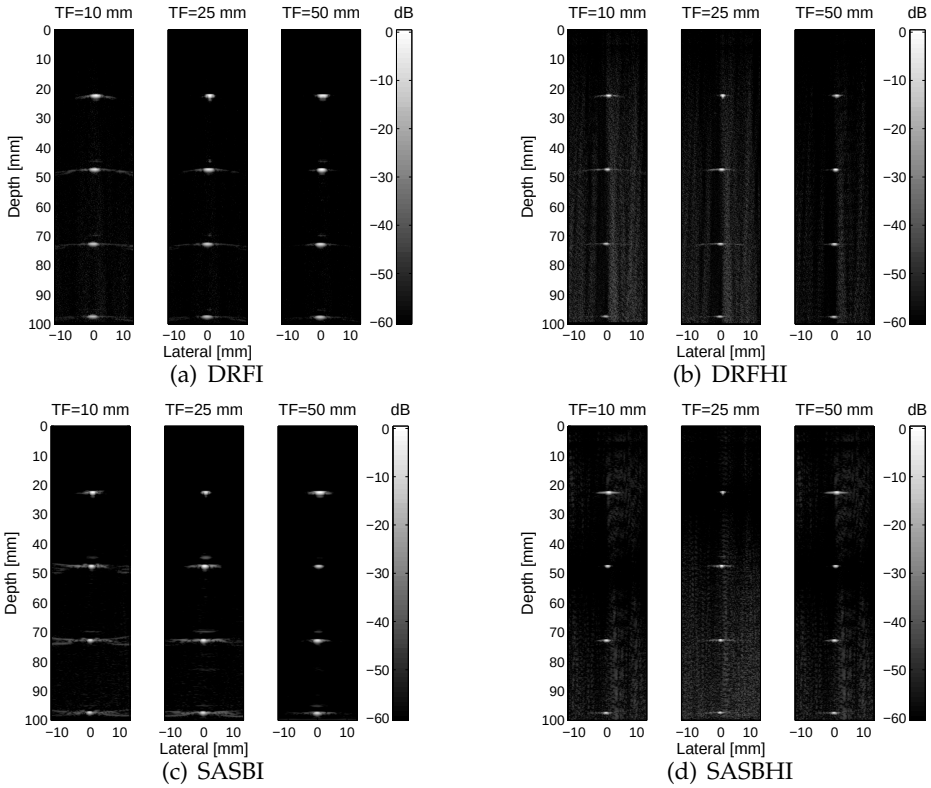

Figure 7.1: Ultrasound images using different methods - DRFI: dynamic receive focus imaging, DRFHI: dynamic receive focus harmonic imaging, SASBI: synthetic aperture sequential beamforming imaging, SASBHI: synthetic aperture sequential beamforming harmonic imaging, TF: transmit focus

focuses in each method. After the evaluation, the ”best” image with an optimized transmit focus is used to compare with other imaging method. The optimization will be simply performed by comparing the FWHM and FWOTH for each point. The narrowest FWHM and FWOTH will get one point, and no point for others. So that there will be eight (4 for FWHM and 4 for FWOTH) comparisons among three transmit focuses. The total score will be divided by its average FWHM in millimeter. The optimization is following the bigger the score, the better the image quality. The final scores are shown in Table 7.3.

In this way, the final comparison with different imaging methods is made among DRFI (TF=50 mm), DRFHI (TF=50 mm), SASBI (TF=10 mm) and SASBHI (TF=10 mm) as show in Fig. 7.2. By calculating the average FWHM and FWOTM for those four points, the lateral resolution of SASBHI

Table 7.1: FWHM of each point in each image and average, - TF is the transmit focus, P1 means the first point along the depth in the image, A is the average FWHM (-6 dB) for those four points

TF	10 mm	25 mm	50 mm	10 mm	25 mm	50 mm
	DRFI			DRFHI		
P1	1.45 mm	0.96 mm	1.94 mm	0.92 mm	0.64 mm	0.78 mm
P2	1.65 mm	1.85 mm	1.35 mm	0.93 mm	1.00 mm	0.80 mm
P3	1.92 mm	1.83 mm	1.76 mm	1.04 mm	1.03 mm	0.95 mm
P4	2.10 mm	1.89 mm	1.88 mm	1.09 mm	1.09 mm	1.01 mm
A	1.78 mm	1.63 mm	1.73 mm	0.99 mm	0.94 mm	0.89 mm
	SASBI			SASBHI		
P1	1.06 mm	0.98 mm	1.72 mm	0.55 mm	0.65 mm	1.06 mm
P2	1.06 mm	1.15 mm	1.38 mm	0.56 mm	0.62 mm	0.88 mm
P3	1.07 mm	1.13 mm	1.38 mm	0.59 mm	0.62 mm	0.85 mm
P4	1.09 mm	1.15 mm	1.36 mm	0.63 mm	0.69 mm	0.89 mm
A	1.07 mm	1.10 mm	1.46 mm	0.58 mm	0.64 mm	0.92 mm

Table 7.2: FWOTM of each point in each image and average, - TF is the transmit focus, P1 means the first point along the depth in the image, A is the average FWOTM (-20 dB) for those four points

TF	10 mm	25 mm	50 mm	10 mm	25 mm	50 mm
	DRFI			DRFHI		
P1	2.92 mm	2.22 mm	2.99 mm	1.61 mm	1.40 mm	1.69 mm
P2	3.12 mm	3.14 mm	2.45 mm	1.71 mm	1.76 mm	1.44 mm
P3	3.25 mm	3.23 mm	3.06 mm	3.40 mm	1.98 mm	1.78 mm
P4	3.40 mm	3.46 mm	3.28 mm	13.0 mm	4.68 mm	2.17 mm
A	3.17 mm	3.01 mm	2.95 mm	4.93 mm	2.45 mm	1.77 mm
	SASBI			SASBHI		
P1	1.84 mm	2.18 mm	3.04 mm	1.00 mm	1.53 mm	2.70 mm
P2	1.91 mm	2.08 mm	2.52 mm	1.15 mm	1.31 mm	1.60 mm
P3	2.00 mm	2.27 mm	2.63 mm	1.58 mm	1.64 mm	1.78 mm
P4	2.27 mm	2.64 mm	2.79 mm	1.98 mm	2.00 mm	1.83 mm
A	2.01 mm	2.29 mm	2.74 mm	1.42 mm	1.62 mm	1.98 mm

is improved by 66%, 35% and 46% for FWHM, and 52%, 20% and 29% for FWOTM compared to DRFI, DRFHI and SASBI, respectively.

To further seek the benefit of SASBHI, the center image lines which go through the point target are plotted for each method for the second wire (P2) as shown in Fig. 7.3. This will have an impact on the axial resolution. The shorter the pulse is, the better the axial resolution can be. To make a comparison, the envelopes of the pulses using these four methods DRFI, DRFHI, SASBI and SASBHI are plotted in Fig. 7.4a. The pulse length becomes narrower for the harmonic imaging. However, the SASBI does not narrow the

Table 7.3: Scores of the image quality using different transmit focuses

TF	10 mm	25 mm	50 mm	10 mm	25 mm	50 mm
	DRFI			DRFHI		
Subscore	0	2	6	0	2	6
A - FWHM	1.78	1.63	1.73	0.99	0.94	0.89
Final score	0	1.23	3.47	0	2.13	6.74
	SASBI			SASBHI		
Subscore	7	1	0	7	0	1
A - FWHM	1.07	1.10	1.46	0.58	0.64	0.92
Final score	6.54	0.91	0	12.1	0	1.09

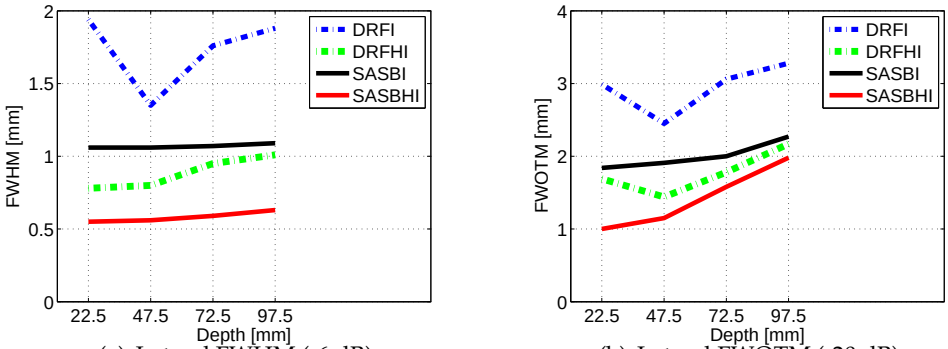

(a) Lateral FWHM (-6 dB) (b) Lateral FWOTM (-20 dB)

Figure 7.2: Full width at -6 dB and -20 dB in lateral - The transmit focus for the DRFI and DRFHI is 50 mm and for the SASBI and SASBHI is 10 mm. The four wires are at the depth of 22.5 mm, 47.5 mm, 72.5 mm and 97.5 mm.

length of the pulse compared to DRFI. More obvious results for the FWHM in axial direction using different imaging methods can be found in Fig. 7.4b. The axial FWHM of SASBHI is improved by 27%, 5% and 25% compared to DRFI, DRFHI and SASBI, respectively.

7.2 Conclusion

In this study, the wire phantom measurement was made by a research scanner SARUS using the BK transducer 8804. Four different imaging algorithms (DRFI, DRFHI, SASBI and SASBHI) were performed using three different transmitting focuses (10 mm, 25 mm and 50 mm from the transducer surface). The combination of SASB and HI results in a much better resolution in the lateral direction than other imaging methods. The improvement for SASBHI can be found at both -6 dB and -20 dB. The axial resolution is also

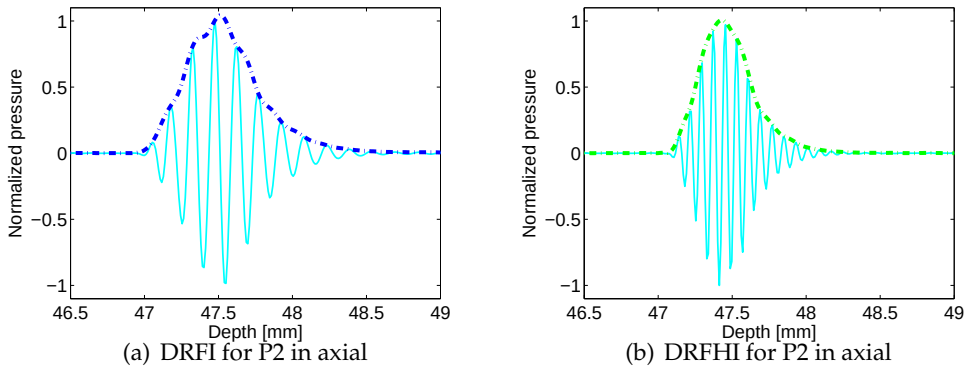

(a) DRFI for P2 in axial

(b) DRFHI for P2 in axial

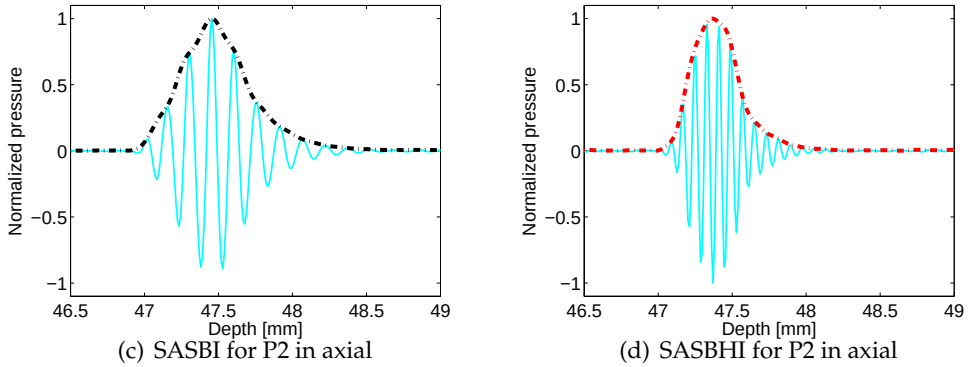

(c) SASBI for P2 in axial

(d) SASBHI for P2 in axial

Figure 7.3: Pulses and envelops in axial using different imaging methods - These show the center image lines for DRFI, DRFHI, SASBI, SASBHI and their envelopes. The plots show the second point target (P2) along the scanning depth and is around 47.5 mm from the transducer surface. The transmit foci is 50 mm for DRFI and DRFHI, and is 10 mm for SASBI and SASBHI.

improved by the HI but only has very little improvement by the SASB from the results.

7.3 Discussion of future developments

This is a preliminary study, since it is the first time that the harmonic signals are beamformed using the SASB. This new idea currently has been investigated that the image quality is indeed improved a lot from the wire phantom measurement. To optimize the SASBHI, there is still a quite long way to go. The lateral resolution is double improved by the SASB and HI, and the axial resolution is only improved by the HI. These have been presented in this

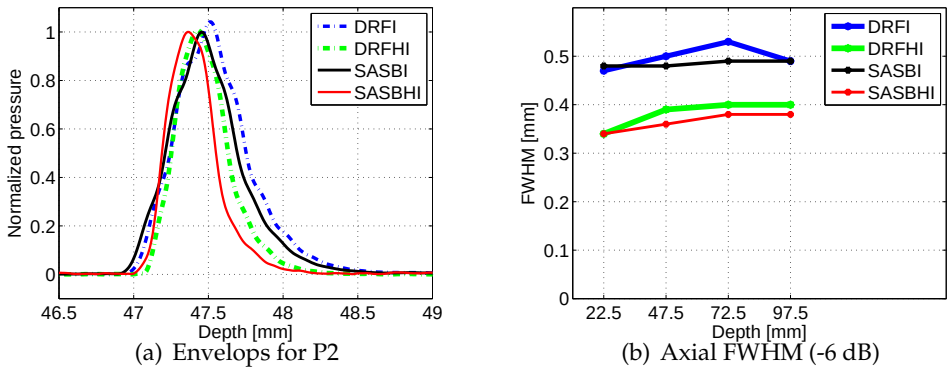

(a) Envelops for P2 (b) Axial FWHM (-6 dB)

Figure 7.4: Envelops and axial FWHM - The envelopes for DRFI, DRFI, SASBI and SASBHI are plotted together in the left figure. The values of the axial FWHM for each method are shown in the right figure.

study. The future development will be based on the sidelobe improvement since it has been observed that the HI can lower the sidelobe. Meanwhile the harmonic signal has lower energy compared to the linear signal, which will decrease the SNR. To get the lower sidelobe by the HI, it is necessary to keep the noise level at least lower than the theoretical harmonic sidelobe level. Otherwise the sidelobe of the HI can become even worse than that of using linear ultrasound imaging. The SNR should be increased and maintain almost the same along the whole image depth for the HI. However, the previous study of SASB by Kortbek [53] showed that the transmit focus is preferred to be close to the transducer surface to get a better resolution from the SASB. In this study, the best transmit focus is 10 mm for SASB. This will make the signals, especially for harmonic signals, become much weeker at the depth far from the transducer surface. This can be found from Fig. 7.2b. The red line (for SASBHI) in Fig. 7.2b goes up much quicker than that in Fig. 7.2a. This is because the SNR is reduced a lot for scanning a target, which is far from the transducer. The low SNR makes the resolution at -20 dB much more influenced by the noise than that at -6 dB. Hence, there will be a compromise to further optimize the image quality from the aspect of the sidelobe and the transmit focal distance.

CHAPTER

EIGHT

Conclusion

Equations for modeling the linear and non-linear acoustic propagation have been derived and presented. The ASA to simulate both the fundamental and second harmonic fields has been successfully implemented in the study. Pulsed ultrasound fields are simulated by the modified ASA, and accuracy is investigated by comparing with Field II for linear ultrasound fields, and by comparing with measurements for non-linear ultrasound fields using geometrically focused piston transducers. The pulsed non-linear ultrasound fields created by a linear array transducer are simulated by the ASA based on Field II, and by Abersim, respectively. The errors of the ASA in this simulation relative to Abersim are within 6.4%. The ASA using the source generated by Field II, makes the non-linear ultrasound simulation flexible to any kind of array transducers with arbitrary focusing, excitation, and apodization. The calculation using ASA is much faster than numerically solving an integral equation using OSM, such as Abersim, since the ASA is an analytical solution and the simulated point can be computed in one step. This makes the optimization of non-linear ultrasound imaging using this simulation approach possible and feasible.

A dual stage harmonic imaging has been presented in the dissertation. The measured results from the preliminary study are showing that the combination of harmonic imaging and SASB gives a great improvement on the lateral resolution. Accordingly, it seems that the axial resolution is only improved by harmonic imaging and hardly by SASB, compared with conventional imaging.

Discussion of future developments

Future work on the non-linear ultrasound should focus on implementing the third harmonic component, where the solution has been derived in Chapter 6. For simulation of strong nonlinearity, a new expression has to be found for the fundamental P_1, since it no longer satisfies the linear propagation. Then each harmonic component can be calculated based on P_1 as shown in (6.9), (6.10), (6.11) and (6.12).

The attenuation part for the ASA should also be included in the future work. This can simply be made by adding an evanescent exponential term in the linear ASA equation (2.48). Then the attenuation for the second harmonic component is also obtained by (A.46). Subsequently, the attenuation terms for each super harmonic component can be found and involved.

The dual stage harmonic imaging will be optimized through the simulation and measurements, which can use a tissue mimicking phantom instead of the wire phantom. This will make the attenuation more realistic and can be assisted by the ASA non-linear simulation.

Bibliography

[1] D. H. Simpson, C. T. Chin, and P. N. Burns. Pulse inversion Doppler: a new method for detecting nonlinear echoes from microbubble contrast agents. *IEEE Trans. Ultrason., Ferroelec., Freq. Contr.*, 46(2):372–382, 1999.

[2] M. A. Averkiou. Tissue harmonic imaging. In *Proc. IEEE Ultrason. Symp.*, volume 2, pages 1563–1572, 2000.

[3] C. S. Chapman and J. C. Lazenby. Ultrasound imaging system employing phase inversion subtraction to enhance the image. *US Patent*, 5632277, 1997.

[4] J. A. Jensen. Medical ultrasound imaging. *Progress in Biophysics and Molecular Biology*, 93:153–165, 2007.

[5] R. T. Beyer. *Nonlinear Acoustics*. Department of the Navy, 1974.

[6] M. F. Hamilton and D. T. Blackstock. *Nonlinear Acoustics*. Academic Press, 1998.

[7] J. A. Jensen and N. B. Svendsen. Calculation of Pressure Fields from Arbitrarily Shaped, Apodized, and Excited Ultrasound Transducers. *IEEE Trans. Ultrason., Ferroelec., Freq. Contr.*, 39:262–267, 1992.

[8] J. A. Jensen. Field: A Program for Simulating Ultrasound Systems. *Med. Biol. Eng. Comp.*, 10th Nordic-Baltic Conference on Biomedical Imaging, Vol. 4, Supplement 1, Part 1:351–353, 1996b.

[9] M. A. Averkiou and M. F. Hamilton. Nonlinear distortion of short pulses radiated by plane and focused circular pistons. *J. Acoust. Soc. Am.*, 102:2539–2548, 1997.

[10] S. I. Aanonsen, T. Barkve, J. N. Tjøtta, and S. Tjøtta. Distortion and harmonic generation in the nearfield of a finite amplitude sound beam. *J. Acoust. Soc. Am.*, 75:749–768, 1984.

[11] M. F. Hamilton, J. N. Tjøtta, and S. Tjøtta. Nonlinear effects in the farfield of a directive sound source. *J. Acoust. Soc. Am.*, 78:202–216, 1985.

[12] J. N. Tjøtta, S. Tjøtta, and E. H. Verfring. Effects of focusing on the nonlinear interaction between two collinear finite amplitude sound beams. *J. Acoust. Soc. Am.*, 89:1017–1027, 1991.

[13] A. C. Baker, A. M. Berg, A. Sahin, and J. N. Tjøtta. The nonlinear pressure field of plane, rectangular apertures: Experimental and theoretical results. *J. Acoust. Soc. Am.*, 97:3510–3517, 1995.

[14] Y.-S. Lee and M. F. Hamilton. Time-domain modeling of pulsed finite-amplitude sound beams. *J. Acoust. Soc. Am.*, 97:906–917, 1995.

[15] J. Tavakkoli, D. Cathignol, and R. Souchon. Modeling of pulsed finite-amplitude focused sound beams in time domain. *J. Acoust. Soc. Am.*, 104:2061–2072, 1998.

[16] J. P. Remenieras, O. Bou Matar, V. Labat, and F. Patat. Time-domain modeling of nonlinear distortion of pulsed finite amplitude sound beams. *Ultrasonics*, 38:305–311, 2000.

[17] L. K. Taylor, M. Schlaikjer, and J. A. Jensen. Modeling of higher harmonics formation in medical ultrasound systems. In *Proc. SPIE - Medical Imaging*, pages 59–67, 2002.

[18] J. A. Jensen, P. D. Fox, J. Wilhjelm, and L. K. Taylor. Simulation of nonlinear ultrasound fields. In *Proc. IEEE Ultrason. Symp.*, volume 2, pages 1733–1736, 2002.

[19] S. Dursun, T. Varslot, T. Johansen, B. Angelsen, and H. Torp. Fast 3D simulation of 2nd harmonic ultrasound field from arbitrary transducer geometries. In *Proc. IEEE Ultrason. Symp.*, pages 1964–1967, 2005.

[20] T. Varslot and G. Taraldsen. Computer simulation of forward wave propagation in soft tissue. *IEEE Trans. Ultrason., Ferroelec., Freq. Contr.*, 52:1473–1482, 2005.

[21] T. Varslot and S. E. Måsøy. Forward propagation of acoustic pressure pulses in 3D soft biological tissue. *IEEE Trans. Ultrason., Ferroelec., Freq. Contr.*, 27:181–200, 2006.

[22] M. E. Frijlink, H. Kaupang, T. Varslot, and S. E. Måsøy. Abersim: a simulation program for 3D nonlinear acoustic wave propagation for arbitrary pulses and arbitrary transducer geometries. In *Proc. IEEE Ultrason. Symp.*, pages 1282–1285, 2008.

[23] H. Kaupang. Abersim 2.x reference manual with tutorials. Technical report, Norwegian University of Science and Technology, Trondheim, Norway, 2008.

[24] E. A. Zabolotskaya and R. V. Khokhlov. Quasi- plane waves in the nonlinear acoustics of confined beams. *Soviet Physics-Acoustics*, 15:35–40, 1969.

[25] V. P. Kuznetsov. Equations of nonlinear acoustics. *Soviet Physics-Acoustics*, 16:467–470, 1971.

[26] P. J. Westervelt. Parametric acoustic array. *J. Acoust. Soc. Am.*, 35:535–537, 1963.

[27] J. M. Burgers. A mathematical model illustrating the theory of turbulence. *Advances in Applied Mechanics*, 1:171–199, 1948.

[28] P. Alais and P. Y. Hennion. A Fourier theory of the nonlinear interaction of acoustical beams in absorbing fluid. The special case of parametric emission. *Acustica*, 43:1–11, 1979.

[29] D. P. Orofino and P. C. Pedersen. Efficient angular spectrum decomposition of acoustic sources-Part I: Theory. *IEEE Trans. Ultrason., Ferroelec., Freq. Contr.*, 40:238–249, 1993.

[30] D. P. Orofino and P. C. Pedersen. Efficient angular spectrum decomposition of acoustic sources-Part II: Results. *IEEE Trans. Ultrason., Ferroelec., Freq. Contr.*, 40:250–257, 1993.

[31] J. W. Goodman. *Introduction to Fourier optics*. McGraw-Hill, 1968.

[32] J. D. Gaskill. *Linear Systems, Fourier Transforms, and Optics(Wiley Series in Pure and Applied Optics)*. Interscience, 1978.

[33] A. Rosenfeld and A. C. Kak. *Digital Picture Processing*. Academic Press, Inc., 2nd edition edition, 1982.

[34] X. Zeng and R. J. McGough. Evaluation of angular spectrum approach for simulations of spherically focused ultrasound phased arrays. *Electro/Information Technology*, pages 66–71, 2006.

[35] X. Zeng and R. J. McGough. Evaluation of the angular spectrum approach for simulations of near-field pressures. *J. Acoust. Soc. Am.*, 123:68–76, 2007.

[36] X. Zeng and R. J. McGough. Optimal simulations of ultrasonic fields produced by large thermal therapy arrays using the angular spectrum approach. *J. Acoust. Soc. Am.*, 125:2967–2977, 2009.

[37] P. Wu and T. Stepinski. Extension of the angular spectrum approach to curved radiators. *J. Acoust. Soc. Am.*, 105:2618–2627, 1999.

[38] P. Wu, R. Kazys, and T. Stepinski. Optimal selection of parameters for the angular spectrum approach to numerically evaluate acoustic fields. *J. Acoust. Soc. Am.*, 101:125–134, 1997.

[39] X. Zhu, L. Zhou, D. Zhang, and X. Gong. Nonlinear propagation of focused ultrasound in layered biological tissues based on angular spectrum approach. *Chinese Physics*, 14(8):1594–1599, 2005.

[40] B. J. Landsberger and M. F. Hamilton. Second-harmonic generation in sound beams reflected from, and transmitted through, immersed elastic solids. *J. Acoust. Soc. Am.*, 109(2):488–500, 2001.

[41] Y. Xiang and M. F. Hamilton. Angular spectrum decomposition analysis of second harmonic ultrasound propagation and its relation to tissue harmonic imaging. In *Ultrasonic and Advanced Methods for Nondestructive Testing and Material Characterization*, pages 11–24, 2006.

[42] L. E. Kinsler, A. R. Frey, A. B. Coppens, and J. V. Sanders. *Fundamentals of Acoustics, 4th edition*. John Wiley and Sons, Inc., New York, 2000.

[43] G. Arfken. *Mathematical method for physicists, 3rd edition*. Academic Press, Orlando, FL.

[44] R. Bracewell. *The Fourier transform and its applications, 3rd edition*. McGraw-Hill, New York.

[45] Y. Xiang. *Statistical model of beam distortion by tissue inhomogeneities in tissue harmonic imaging*. PhD thesis, University of Texas at Austin, Texas, USA, 2004.

[46] Y. Du and J. A. Jensen. Feasibility of non-linear simulation for Field II using an angular spectrum approach. In *Proc. IEEE Ultrason. Symp.*, pages 1314–1317, 2008.

[47] Y. Du, H. Jensen, and J. A. Jensen. Simulation of second harmonic ultrasound fields. In *Proc. IEEE Ultrason. Symp.*, 2010.

[48] Y. Du, H. Jensen, and J. A. Jensen. Comparison of simulated and measured non-linear ultrasound fields. In *Proc. SPIE - Medical Imaging*, pages 79680P, 1–10, 2011.

[49] J. A. Jensen. User guide for the Field II program. Technical report, Technical University of Denmark, Lyngby, Denmark, 2001.

[50] C. Shannon. Communication in the presence of noise. In *IEEE*, volume 37, pages 10–21, 1949.

[51] M. Bae, H. Lee, S. B. Park, R. Yoon, M. H. Jeong, D. G. Kim, M. Jeong, and Y. Kim. A new ultrasonic synthetic aperture tissue harmonic imaging system. In *Proc. IEEE Ultrason. Symp.*, pages 1258–1261, 2008.

[52] J. Kortbek, J. A. Jensen, and K. L. Gammelmark. Sequential beamforming - an efficient synthetic aperture technique. *IEEE Trans. Ultrason., Ferroelec., Freq. Contr.*, 2010.

[53] J. Kortbek. *Synthetic aperture sequential beamforming and other beamforming techniques in ultrasound imaging*. PhD thesis, Technical University of Denmark, Lyngby, Denmark, 2007.

[54] J. Kortbek, J. A. Jensen, and K. L. Gammelmark. Synthetic aperture sequential beamforming. In *Proc. IEEE Ultrason. Symp.*, pages 966–969, 2008.

[55] J. A. Jensen, H. Holten-Lund, R. T. Nielson, B. G. Tomov, M. B. Stuart, S. I. Nikolov, M. Hansen, and U. D. Larsen. Performance of SARUS: a synthetic aperture real-time ultrasound system. In *Proc. IEEE Ultrason. Symp.*, 2010.

[56] J. Kortbek, S. I. Nikolov, and J. A. Jensen. Effective and Versatile software Beamformation Toolbox. In *Proc. SPIE - Medical Imaging - Ultrasonic Imaging and Signal Processsing*, pages 651319, 1–10, 2007.

[57] S. Gustavsson and J. Kortbek. User guide for the beamformation toolbox II, release 9.0. Technical report, Technical University of Denmark, Lyngby, Denmark, 2009.

APPENDIX

A

Derivation of equations

A.1 Description for Equation (2.32)

A one-dimensional linear wave equation can be expressed by

$$\frac{\partial^2 u}{\partial x^2} = \frac{1}{c^2}\frac{\partial^2 u}{\partial t^2}, \tag{A.1}$$

Characteristics of (A.1) is defined by

$$\left(\frac{\partial F}{\partial t}\right)^2 - c^2\left(\frac{\partial F}{\partial x}\right)^2 = 0. \tag{A.2}$$

Simplify (A.2),

$$\frac{\partial F}{\partial t} = \pm c\frac{\partial F}{\partial x}, \tag{A.3}$$

thus

$$F = f_1(ct + x) + f_2(ct - x). \tag{A.4}$$

According to (A.4), make the following coordinate transformation by

$$\xi_1 = ct + x, \tag{A.5}$$
$$\xi_2 = ct - x. \tag{A.6}$$

Taking derivative for (A.5) and (A.6) with respect to x and t, respectively gives to

$$\frac{\partial \xi_1}{\partial x} = 1 \quad , \qquad \frac{\partial \xi_1}{\partial t} = c, \tag{A.7}$$
$$\frac{\partial \xi_2}{\partial x} = -1, \qquad \frac{\partial \xi_2}{\partial t} = c. \tag{A.8}$$

By use of (A.1), (A.7) and (A.8), write down the following derivation using the chain rule

$$\frac{\partial u}{\partial x} = \frac{\partial u}{\partial \xi_1}\frac{\partial \xi_1}{\partial x} + \frac{\partial u}{\partial \xi_2}\frac{\partial \xi_2}{\partial x} = \frac{\partial u}{\partial \xi_1} - \frac{\partial u}{\partial \xi_2}, \tag{A.9}$$

$$\frac{\partial u}{\partial t} = \frac{\partial u}{\partial \xi_1}\frac{\partial \xi_1}{\partial t} + \frac{\partial u}{\partial \xi_2}\frac{\partial \xi_2}{\partial t} = c\left(\frac{\partial u}{\partial \xi_1} + \frac{\partial u}{\partial \xi_2}\right). \tag{A.10}$$

The second order derivatives are given by

$$\begin{aligned}\frac{\partial^2 u}{\partial x^2} &= \frac{\partial}{\partial x}\left(\frac{\partial u}{\partial \xi_1} - \frac{\partial u}{\partial \xi_2}\right) \\ &= \left[\frac{\partial}{\partial \xi_1}\left(\frac{\partial u}{\partial \xi_1}\right)\right]\left(\frac{\partial \xi_1}{\partial x}\right) + \left[\frac{\partial}{\partial \xi_2}\left(\frac{\partial u}{\partial \xi_1}\right)\right]\left(\frac{\partial \xi_2}{\partial x}\right) \\ &\quad - \left[\frac{\partial}{\partial \xi_1}\left(\frac{\partial u}{\partial \xi_2}\right)\right]\left(\frac{\partial \xi_1}{\partial x}\right) - \left[\frac{\partial}{\partial \xi_2}\left(\frac{\partial u}{\partial \xi_2}\right)\right]\left(\frac{\partial \xi_2}{\partial x}\right) \\ &= \frac{\partial^2 u}{\partial \xi_1^2} + \frac{\partial^2 u}{\partial \xi_2^2} - 2\frac{\partial^2 u}{\partial \xi_1 \partial \xi_2},\end{aligned} \tag{A.11}$$

$$\begin{aligned}\frac{\partial^2 u}{\partial t^2} &= c\frac{\partial}{\partial t}\left(\frac{\partial u}{\partial \xi_1} + \frac{\partial u}{\partial \xi_2}\right) \\ &= c\left[\frac{\partial}{\partial \xi_1}\left(\frac{\partial u}{\partial \xi_1}\right)\right]\left(\frac{\partial \xi_1}{\partial t}\right) + c\left[\frac{\partial}{\partial \xi_2}\left(\frac{\partial u}{\partial \xi_1}\right)\right]\left(\frac{\partial \xi_2}{\partial t}\right) \\ &\quad + c\left[\frac{\partial}{\partial \xi_1}\left(\frac{\partial u}{\partial \xi_2}\right)\right]\left(\frac{\partial \xi_1}{\partial t}\right) + c\left[\frac{\partial}{\partial \xi_2}\left(\frac{\partial u}{\partial \xi_2}\right)\right]\left(\frac{\partial \xi_2}{\partial t}\right) \\ &= c^2\frac{\partial^2 u}{\partial \xi_1^2} + c^2\frac{\partial^2 u}{\partial \xi_2^2} + 2c^2\frac{\partial^2 u}{\partial \xi_1 \partial \xi_2}.\end{aligned} \tag{A.12}$$

Substituting (A.11) and (A.12) into (A.1) results to

$$\frac{\partial^2 u}{\partial \xi_1 \partial \xi_2} = 0. \tag{A.13}$$

This is called the second canonical form for the hyperbolic PDE (partial differential equation) denoting that there is no $\xi_1 \cdot \xi_2$ term in the solution. Therefore, the general solution can be expressed by

$$u = F_1(\xi_1) + F_2(\xi_2). \tag{A.14}$$

F_1 and F_2 are arbitrary functions, which may be $(t \pm x/c)^2$, $sin[\omega(t \pm x/c)]$, $log(ct \pm x)$, $exp[jk(ct \pm x)]$ and so on. This is for the acoustic wave propagating in a one-dimensional space. Similarly it can be proved that there is no $t \cdot x$, $t \cdot y$ and $t \cdot z$ terms in the solution either while the acoustic wave propagates in the three-dimensional space. Therefore, a separate variable solution can be expressed and given by (2.32).

A.2 Derivation for Equation (2.51)

The equation derivations from (2.50) to (2.51) is similar to that from (2.36) to (2.43). Taking the two-dimensional spatial Fourier transform on both sides of (2.50) gives to

$$\iint (\nabla^2 + 4k^2) P_2(x, y, z_1) e^{-j(k_x x + k_y y)} dx dy = \frac{\beta k^2}{2\pi^2 \rho_0 c_0^2} \iint \hat{P}_1(k'_x, k'_y, z_1) \times \hat{P}_1(k_x - k'_x, k_y - k'_y, z_1) dk'_x dk'_y. \tag{A.15}$$

Substituting (2.48) into (A.15) gives to

$$\iint (\nabla^2 + 4k^2) P_2(x, y, z_1) e^{-j(k_x x + k_y y)} dx dy = \frac{\beta k^2}{2\pi^2 \rho_0 c_0^2} M(k_x, k_y, z_1), \tag{A.16}$$

where

$$\begin{aligned} M(k_x, k_y, z_1) &= \iint e^{-j(z_1 - z_0)(k'_z + k''_z)} \hat{P}_0(k'_x, k'_y, z_0) \\ &\quad \times \hat{P}_0(k_x - k'_x, k_y - k'_y, z_0) dk'_x dk'_y, && \text{(A.17)} \\ k'_z &= \sqrt{k^2 - (k'_x)^2 - (k'_y)^2}, && \text{(A.18)} \\ k''_z &= \sqrt{k^2 - (k_x - k'_x)^2 - (k_y - k'_y)^2}. && \text{(A.19)} \end{aligned}$$

Substituting (2.39) into (A.16) gives to

$$\iint (\nabla^2 + 4k^2) \left[\frac{1}{(2\pi)^2} \iint \hat{P}_2(k_x, k_y, z_1) e^{j(k_x x + k_y y)} dk_x dk_y \right] e^{-j(k_x x + k_y y)} dx dy = \frac{\beta k^2}{2\pi^2 \rho_0 c_0^2} M(k_x, k_y, z_1), \tag{A.20}$$

Further derivation for (A.20) by splitting each term of the left hand side and given by

$$\iint (T_A + T_B) e^{-j(k_x x + k_y y)} dx dy = \frac{\beta k^2}{2\pi^2 \rho_0 c_0^2} M(k_x, k_y, z_1), \tag{A.21}$$

where

$$\begin{aligned} T_A &= \nabla^2 \left[\frac{1}{(2\pi)^2} \iint \hat{P}_2(k_x, k_y, z_1) e^{j(k_x x + k_y y)} dk_x dk_y \right], && \text{(A.22)} \\ T_B &= 4k^2 \left[\frac{1}{(2\pi)^2} \iint \hat{P}_2(k_x, k_y, z_1) e^{j(k_x x + k_y y)} dk_x dk_y \right], && \text{(A.23)} \end{aligned}$$

T_A can be derived by

$$\begin{aligned} T_A &= \nabla^2 \left[\frac{1}{(2\pi)^2} \iint \hat{P}_2(k_x, k_y, z_1) e^{j(k_x x + k_y y)} dk_x dk_y \right] \\ &= \frac{1}{(2\pi)^2} \iint \nabla^2 \left[\hat{P}_2(k_x, k_y, z_1) e^{j(k_x x + k_y y)} \right] dk_x dk_y \\ &= \frac{1}{(2\pi)^2} \iint \left(T_{A1} + T_{A2} + T_{A3} \right) dk_x dk_y \end{aligned} \tag{A.24}$$

where

$$T_{A1} = \frac{\partial^2}{\partial x^2} \left[\hat{P}_2(k_x, k_y, z_1) e^{j(k_x x + k_y y)} \right] = -k_x^2 \hat{P}_2(k_x, k_y, z_1) e^{j(k_x x + k_y y)}, \tag{A.25}$$

$$T_{A2} = \frac{\partial^2}{\partial y^2} \left[\hat{P}_2(k_x, k_y, z_1) e^{j(k_x x + k_y y)} \right] = -k_y^2 \hat{P}_2(k_x, k_y, z_1) e^{j(k_x x + k_y y)}, \tag{A.26}$$

$$T_{A3} = \frac{\partial^2}{\partial z^2} \left[\hat{P}_2(k_x, k_y, z_1) e^{j(k_x x + k_y y)} \right] = \frac{\partial^2 \hat{P}_2(k_x, k_y, z_1)}{\partial z^2} e^{j(k_x x + k_y y)}. \tag{A.27}$$

Substituting the simplified T_{A1}, T_{A2} and T_{A3} into T_A, (A.24) can be rewritten by

$$T_A = \frac{1}{(2\pi)^2} \iint \left[\left(\frac{\partial^2}{\partial z^2} - k_x^2 - k_y^2 \right) \hat{P}_2(k_x, k_y, z_1) \right] e^{j(k_x x + k_y y)} dk_x dk_y. \tag{A.28}$$

T_B can be derived by

$$\begin{aligned} T_B &= 4k^2 \left[\frac{1}{(2\pi)^2} \iint \hat{P}_2(k_x, k_y, z_1) e^{j(k_x x + k_y y)} dk_x dk_y \right], \\ &= \frac{1}{(2\pi)^2} \iint 4k^2 \hat{P}_2(k_x, k_y, z_1) e^{j(k_x x + k_y y)} dk_x dk_y. \end{aligned} \tag{A.29}$$

Substituting the simplified T_A - (A.28) and T_B - (A.29) into (A.21) gives to

$$\begin{aligned} &\iint \left[\frac{1}{(2\pi)^2} \iint T_C e^{j(k_x x + k_y y)} dk_x dk_y \right] e^{-j(k_x x + k_y y)} dx dy \\ &\qquad = \frac{\beta k^2}{2\pi^2 \rho_0 c_0^2} M(k_x, k_y, z_1), \end{aligned} \tag{A.30}$$

where

$$T_C = \left(\frac{\partial^2}{\partial z^2} - k_x^2 - k_y^2 + 4k^2 \right) \hat{P}_2(k_x, k_y, z_1). \tag{A.31}$$

The left hand side of (A.30) is T_C itself after forward and inverse Fourier transforms. Finally, (A.30) can be expressed by

$$\left(\frac{\partial^2}{\partial z^2} + 4k^2 - k_x^2 - k_y^2\right)\hat{P}_2(k_x, k_y, z_1) = \frac{\beta k^2}{2\pi^2 \rho_0 c_0^2} M(k_x, k_y, z_1). \tag{A.32}$$

A.3 Derivation of the Solution Equation (2.56)

The solution to an inhomogeneous ordinary differential equation (2.51), should be comprised of a general solution for the homogeneous differential equation as well as a particular solution. This can be expressed by

$$\hat{P}_2(k_x, k_y, z) = Ae^{-jk_{z2}z} + Be^{jk_{z2}z} + \hat{P}_{2p}(k_x, k_y, z). \tag{A.33}$$

To simplify (2.51) and find the particular solution, it can be assumed that

$$\hat{P}_{2p}(k_x, k_y, z) = \bar{P}_{2p}(k_x, k_y, z)e^{-jk_{z2}z}, \tag{A.34}$$

Substituting the particular solution (A.34) into (2.51) gives to

$$\left(\frac{d^2}{dz^2} + k_{z2}^2\right)\left[\bar{P}_{2p}(k_x, k_y, z)e^{-jk_{z2}z}\right] = \eta M(k_x, k_y, z), \tag{A.35}$$

where

$$\eta = \frac{\beta k^2}{2\pi^2 \rho_0 c_0^2}. \tag{A.36}$$

The left hand side of (A.35) can be further derived by

$$\begin{aligned} L_{\text{A.35}} &= \frac{d^2}{dz^2}\left[\bar{P}_{2p}(k_x, k_y, z)e^{-jk_{z2}z}\right] + k_{z2}^2\left[\bar{P}_{2p}(k_x, k_y, z)e^{-jk_{z2}z}\right] \\ &= \frac{d}{dz}\left\{\frac{d}{dz}\left[\bar{P}_{2p}(k_x, k_y, z)e^{-jk_{z2}z}\right]\right\} + k_{z2}^2\bar{P}_{2p}(k_x, k_y, z)e^{-jk_{z2}z} \\ &= \frac{d}{dz}\left[\frac{d\bar{P}_{2p}}{dz}e^{-jk_{z2}z} - jk_{z2}\bar{P}_{2p}e^{-jk_{z2}z}\right] + k_{z2}^2\bar{P}_{2p}e^{-jk_{z2}z} \\ &= \frac{d^2\bar{P}_{2p}}{dz^2}e^{-jk_{z2}z} - 2jk_{z2}e^{-jk_{z2}z}\frac{d\bar{P}_{2p}}{dz}. \end{aligned} \tag{A.37}$$

Therefore, (A.35) is rewritten by

$$\frac{d^2\bar{P}_{2p}}{dz^2} - 2jk_{z2}\frac{d\bar{P}_{2p}}{dz} = \eta M e^{jk_{z2}z}. \tag{A.38}$$

Substituting $Q = d\bar{P}_{2p}/dz$ into (A.38) gives to

$$\frac{dQ}{dz} - 2jk_{z2}Q = \eta M e^{jk_{z2}z}. \tag{A.39}$$

Substituting $Q = \bar{Q}e^{j2k_{z2}z}$ into (A.39) gives to

$$\begin{aligned} \frac{d}{dz}\left(\bar{Q}e^{j2k_{z2}z}\right) - 2jk_{z2}\left(\bar{Q}e^{j2k_{z2}z}\right) &= \eta M e^{jk_{z2}z} \\ \frac{d\bar{Q}}{dz} &= \eta M e^{-jk_{z2}z}. \end{aligned} \tag{A.40}$$

The solution to (A.40) is given by

$$\bar{Q} = \eta \int M e^{-jk_{z2}z} dz + C_1, \tag{A.41}$$

where C_1 is a constant. Using $Q = \bar{Q}e^{j2k_{z2}z}$ again, (A.41) can be rewritten by

$$Q = \eta e^{j2k_{z2}z} \int M e^{-jk_{z2}z} dz + C_1 e^{j2k_{z2}z}. \tag{A.42}$$

Using $Q = d\bar{P}_{2p}/dz$ again, (A.42) becomes

$$\frac{d\bar{P}_{2p}}{dz} = \eta e^{j2k_{z2}z} \int M e^{-jk_{z2}z} dz + C_1 e^{j2k_{z2}z}. \tag{A.43}$$

The solution to (A.43) is given by

$$\bar{P}_{2p} = \eta \int \left[e^{j2k_{z2}z} \left(\int M e^{-jk_{z2}z} dz \right) + C_1 e^{j2k_{z2}z} \right] dz + C_2, \tag{A.44}$$

where C_2 is a constant as well. Substituting (A.44) into (A.34) gives to

$$\begin{aligned} \hat{P}_{2p} &= \eta e^{-jk_{z2}z} \int \left[e^{j2k_{z2}z} \left(\int M e^{-jk_{z2}z} dz \right) + C_1 e^{j2k_{z2}z} \right] dz + C_2 e^{-jk_{z2}z} \\ &= \eta e^{-jk_{z2}z} \left\{ \int \left[e^{j2k_{z2}z} \int M e^{-jk_{z2}z} dz \right] dz + \int C_1 e^{j2k_{z2}z} dz \right\} \\ &\quad + C_2 e^{-jk_{z2}z} \\ &= \eta e^{-jk_{z2}z} \left\{ \int \left[e^{j2k_{z2}z} \int M e^{-jk_{z2}z} dz \right] dz \right\} + C_3 e^{-jk_{z2}z} \int e^{j2k_{z2}z} dz \\ &\quad + C_2 e^{-jk_{z2}z} \\ &= \eta e^{-jk_{z2}z} \left\{ \int \left[e^{j2k_{z2}z} \int M e^{-jk_{z2}z} dz \right] dz \right\} + C_4 e^{jk_{z2}z} + C_2 e^{-jk_{z2}z} \end{aligned} \tag{A.45}$$

The last two terms in (A.45) can be merged into the first two terms in (A.33). It is assumed that the acoustic wave is propagated along $+z$ direction and the term with $e^{jk_{z2}z}$ is eliminated. Thus, by use of (2.52), $\hat{P}_2(k_x, k_y, z)$ at $z = z_1$ can be written as

$$
\begin{aligned}
\hat{P}_2 &= Ae^{-jk_{z2}z_1} + \eta e^{-jk_{z2}z_1} \int_{z_0}^{z_1} e^{j2k_{z2}z_1'} \int_{z_0}^{z_1'} e^{-jk_{z2}z} \iint e^{-j(z-z_0)(k_z'+k_z'')} \\
&\quad \times \hat{P}_0(k_x', k_y', z_0) \times \hat{P}_0(k_x - k_x', k_y - k_y', z_0) dk_x' dk_y' dz dz_1' \\
&= Ae^{-jk_{z2}z_1} + \eta \iint e^{-jk_{z2}(z_1-z_0)} \int_{z_0}^{z_1} e^{j2k_{z2}(z_1'-z_0)} \int_{z_0}^{z_1'} e^{-j(z-z_0)(k_z'+k_z'')} \\
&\quad \times e^{-jk_{z2}(z-z_0)} dz dz_1' \hat{P}_0(k_x', k_y', z_0) \times \hat{P}_0(k_x - k_x', k_y - k_y', z_0) dk_x' dk_y'. \\
&= Ae^{-jk_{z2}z_1} + \eta \iint e^{-jk_{z2}(z_1-z_0)} \int_{z_0}^{z_1} e^{j2k_{z2}(z_1'-z_0)} \\
&\quad \times \int_{z_0}^{z_1'} e^{-j(z-z_0)(k_{z2}+k_z'+k_z'')} dz dz_1' \hat{P}_0(k_x', k_y', z_0) \\
&\quad \times \hat{P}_0(k_x - k_x', k_y - k_y', z_0) dk_x' dk_y' \\
&= Ae^{-jk_{z2}z_1} + \eta \iint e^{-jk_{z2}(z_1-z_0)} \int_{z_0}^{z_1} e^{j2k_{z2}(z_1'-z_0)} \\
&\quad \times \frac{e^{-j(z_1'-z_0)(k_{z2}+k_z'+k_z'')} - 1}{-j(k_{z2}+k_z'+k_z'')} dz_1' \hat{P}_0(k_x', k_y', z_0) \\
&\quad \times \hat{P}_0(k_x - k_x', k_y - k_y', z_0) dk_x' dk_y' \\
&= Ae^{-jk_{z2}z_1} + \eta \iint e^{-jk_{z2}(z_1-z_0)} \\
&\quad \times \int_{z_0}^{z_1} \frac{e^{j(z_1'-z_0)(k_{z2}-k_z'-k_z'')} - e^{j2k_{z2}(z_1'-z_0)}}{-j(k_{z2}+k_z'+k_z'')} dz_1' \\
&\quad \times \hat{P}_0(k_x', k_y', z_0) \hat{P}_0(k_x - k_x', k_y - k_y', z_0) dk_x' dk_y' \\
&= Ae^{-jk_{z2}z_1} + \eta \iint e^{-jk_{z2}(z_1-z_0)} \\
&\quad \times \left[\frac{e^{j(z_1-z_0)(k_{z2}-k_z'-k_z'')} - 1}{(k_{z2}+k_z'+k_z'')(k_{z2}-k_z'-k_z'')} - \frac{e^{j2k_{z2}(z_1-z_0)} - 1}{2k_{z2}(k_{z2}+k_z'+k_z'')} \right] \\
&\quad \times \hat{P}_0(k_x', k_y', z_0) \hat{P}_0(k_x - k_x', k_y - k_y', z_0) dk_x' dk_y' \\
&= Ae^{-jk_{z2}z_1} + \eta \iint \hat{P}_0(k_x', k_y', z_0) \\
&\quad \times \left[\frac{e^{-j(z_1-z_0)(k_z'+k_z'')} - e^{-jk_{z2}(z_1-z_0)}}{(k_{z2}+k_z'+k_z'')(k_{z2}-k_z'-k_z'')} - \frac{e^{jk_{z2}(z_1-z_0)} - e^{-jk_{z2}(z_1-z_0)}}{2k_{z2}(k_{z2}+k_z'+k_z'')} \right] \\
&\quad \times \hat{P}_0(k_x - k_x', k_y - k_y', z_0) dk_x' dk_y'
\end{aligned}
\tag{A.46}
$$

The term with $e^{jk_{z2}z}$ from (A.46) is removed again due to the forward propagation. Thus, (A.46) becomes

$$\begin{aligned}\hat{P}_2(k_x,k_y,z_1) =& Ae^{-jk_{z2}z_1} + \eta \iint \hat{P}_0(k'_x,k'_y,z_0) \\ &\times \left[\frac{e^{-j(z_1-z_0)(k'_z+k''_z)} - e^{-jk_{z2}(z_1-z_0)}}{(k_{z2}+k'_z+k''_z)(k_{z2}-k'_z-k''_z)} + \frac{e^{-jk_{z2}(z_1-z_0)}}{2k_{z2}(k_{z2}+k'_z+k''_z)}\right] \\ &\times \hat{P}_0(k_x-k'_x,k_y-k'_y,z_0)dk'_xdk'_y \end{aligned} \tag{A.47}$$

It is assumed that the acoustic source has no non-linear effect, which can be expressed by

$$\hat{P}_2(k_x,k_y,z_0) = 0. \tag{A.48}$$

Substituting $z_1 = z_0$ into (A.47) gives to

$$\begin{aligned}\hat{P}_2(k_x,k_y,z_0) &= Ae^{-jk_{z2}z_0} + \eta \iint \hat{P}_0(k'_x,k'_y,z_0)\hat{P}_0(k_x-k'_x,k_y-k'_y,z_0) \\ &\times \frac{1}{2k_{z2}(k_{z2}+k'_z+k''_z)}dk'_xdk'_y. \end{aligned} \tag{A.49}$$

With (A.48), (A.49) becomes

$$\begin{aligned}A &= -\eta e^{jk_{z2}z_0} \iint \hat{P}_0(k'_x,k'_y,z_0)\hat{P}_0(k_x-k'_x,k_y-k'_y,z_0) \\ &\times \frac{1}{2k_{z2}(k_{z2}+k'_z+k''_z)}dk'_xdk'_y. \end{aligned} \tag{A.50}$$

Substituting (A.50) and (A.36) into (A.47) results in

$$\begin{aligned}\hat{P}_2(k_x,k_y,z_1) &= \frac{\beta k^2}{2\pi^2\rho_0 c_0^2} \iint \frac{e^{-j(z_1-z_0)(k'_z+k''_z)} - e^{-j(z_1-z_0)k_{z2}}}{k_{z2}^2-(k'_z+k''_z)^2}\hat{P}_0(k'_x,k'_y,z_0) \\ &\times \hat{P}_0(k_x-k'_x,k_y-k'_y,z_0)dk'_xdk'_y. \end{aligned} \tag{A.51}$$

This is the final solution which is derived by the ASA for monochromatic fields with constant k.

A.4 Discrete Implementing Equations

There are 16 discrete implementing equations. For different cases, $\mathrm{DI}(m_x,m_y,n_f)$ can be expressed by

When $f<0$, $4k^2>k_x^2+k_y^2$, $k^2>(k_x')^2+(k_y')^2$, $k^2>(k_x-k_x')^2+(k_y-k_y')^2$

$$\begin{aligned}\text{DI} &= \frac{1}{N_xN_y}\sum_{n_y=0}^{N_y-1}\sum_{n_x=0}^{N_x-1}\hat{P}_{d0}(n_x,n_y,n_f)\hat{P}_{d0}(m_x-n_x,m_y-n_y,n_f)\\ &\times\frac{e^{j(z_1-z_0)[k_z'(n_x,n_y)+k_z''(m_x-n_x,m_y-n_y)]}-e^{j(z_1-z_0)k_{z2}(m_x,m_y)}}{k_{z2}^2(m_x,m_y)-[k_z'(n_x,n_y)+k_z''(m_x-n_x,m_y-n_y)]^2},\\ &(m_x=0,...M_x-1,\quad m_y=0,...M_y-1)\end{aligned}\tag{A.52}$$

When $f<0$, $4k^2>k_x^2+k_y^2$, $k^2>(k_x')^2+(k_y')^2$, $k^2\le(k_x-k_x')^2+(k_y-k_y')^2$

$$\begin{aligned}\text{DI} &= \frac{1}{N_xN_y}\sum_{n_y=0}^{N_y-1}\sum_{n_x=0}^{N_x-1}\hat{P}_{d0}(n_x,n_y,n_f)\hat{P}_{d0}(m_x-n_x,m_y-n_y,n_f)\\ &\times\frac{e^{(z_1-z_0)[jk_z'(n_x,n_y)-k_z''(m_x-n_x,m_y-n_y)]}-e^{j(z_1-z_0)k_{z2}(m_x,m_y)}}{k_{z2}^2(m_x,m_y)-[k_z'(n_x,n_y)+k_z''(m_x-n_x,m_y-n_y)]^2},\\ &(m_x=0,...M_x-1,\quad m_y=0,...M_y-1)\end{aligned}\tag{A.53}$$

When $f<0$, $4k^2>k_x^2+k_y^2$, $k^2\le(k_x')^2+(k_y')^2$, $k^2>(k_x-k_x')^2+(k_y-k_y')^2$

$$\begin{aligned}\text{DI} &= \frac{1}{N_xN_y}\sum_{n_y=0}^{N_y-1}\sum_{n_x=0}^{N_x-1}\hat{P}_{d0}(n_x,n_y,n_f)\hat{P}_{d0}(m_x-n_x,m_y-n_y,n_f)\\ &\times\frac{e^{(z_1-z_0)[-k_z'(n_x,n_y)+jk_z''(m_x-n_x,m_y-n_y)]}-e^{j(z_1-z_0)k_{z2}(m_x,m_y)}}{k_{z2}^2(m_x,m_y)-[k_z'(n_x,n_y)+k_z''(m_x-n_x,m_y-n_y)]^2},\\ &(m_x=0,...M_x-1,\quad m_y=0,...M_y-1)\end{aligned}\tag{A.54}$$

When $f<0$, $4k^2>k_x^2+k_y^2$, $k^2\le(k_x')^2+(k_y')^2$, $k^2\le(k_x-k_x')^2+(k_y-k_y')^2$

$$\begin{aligned}\text{DI} &= \frac{1}{N_xN_y}\sum_{n_y=0}^{N_y-1}\sum_{n_x=0}^{N_x-1}\hat{P}_{d0}(n_x,n_y,n_f)\hat{P}_{d0}(m_x-n_x,m_y-n_y,n_f)\\ &\times\frac{e^{-(z_1-z_0)[k_z'(n_x,n_y)+k_z''(m_x-n_x,m_y-n_y)]}-e^{j(z_1-z_0)k_{z2}(m_x,m_y)}}{k_{z2}^2(m_x,m_y)-[k_z'(n_x,n_y)+k_z''(m_x-n_x,m_y-n_y)]^2},\\ &(m_x=0,...M_x-1,\quad m_y=0,...M_y-1)\end{aligned}\tag{A.55}$$

When $f<0$, $4k^2 \le k_x^2+k_y^2$, $k^2 > (k_x')^2+(k_y')^2$, $k^2 > (k_x-k_x')^2+(k_y-k_y')^2$

$$\begin{aligned}\mathrm{DI} &= \frac{1}{N_xN_y}\sum_{n_y=0}^{N_y-1}\sum_{n_x=0}^{N_x-1}\hat{P}_{d_0}(n_x,n_y,n_f)\hat{P}_{d_0}(m_x-n_x,m_y-n_y,n_f)\\ &\times\frac{e^{j(z_1-z_0)[k_z'(n_x,n_y)+k_z''(m_x-n_x,m_y-n_y)]}-e^{-(z_1-z_0)k_{z2}(m_x,m_y)}}{k_{z2}^2(m_x,m_y)-\left[k_z'(n_x,n_y)+k_z''(m_x-n_x,m_y-n_y)\right]^2},\\ &(m_x=0,...M_x-1,\quad m_y=0,...M_y-1)\end{aligned} \tag{A.56}$$

When $f<0$, $4k^2 \le k_x^2+k_y^2$, $k^2 > (k_x')^2+(k_y')^2$, $k^2 \le (k_x-k_x')^2+(k_y-k_y')^2$

$$\begin{aligned}\mathrm{DI} &= \frac{1}{N_xN_y}\sum_{n_y=0}^{N_y-1}\sum_{n_x=0}^{N_x-1}\hat{P}_{d_0}(n_x,n_y,n_f)\hat{P}_{d_0}(m_x-n_x,m_y-n_y,n_f)\\ &\times\frac{e^{(z_1-z_0)[jk_z'(n_x,n_y)-k_z''(m_x-n_x,m_y-n_y)]}-e^{-(z_1-z_0)k_{z2}(m_x,m_y)}}{k_{z2}^2(m_x,m_y)-\left[k_z'(n_x,n_y)+k_z''(m_x-n_x,m_y-n_y)\right]^2},\\ &(m_x=0,...M_x-1,\quad m_y=0,...M_y-1)\end{aligned} \tag{A.57}$$

When $f<0$, $4k^2 \le k_x^2+k_y^2$, $k^2 \le (k_x')^2+(k_y')^2$, $k^2 > (k_x-k_x')^2+(k_y-k_y')^2$

$$\begin{aligned}\mathrm{DI} &= \frac{1}{N_xN_y}\sum_{n_y=0}^{N_y-1}\sum_{n_x=0}^{N_x-1}\hat{P}_{d_0}(n_x,n_y,n_f)\hat{P}_{d_0}(m_x-n_x,m_y-n_y,n_f)\\ &\times\frac{e^{(z_1-z_0)[-k_z'(n_x,n_y)+jk_z''(m_x-n_x,m_y-n_y)]}-e^{-(z_1-z_0)k_{z2}(m_x,m_y)}}{k_{z2}^2(m_x,m_y)-\left[k_z'(n_x,n_y)+k_z''(m_x-n_x,m_y-n_y)\right]^2},\\ &(m_x=0,...M_x-1,\quad m_y=0,...M_y-1)\end{aligned} \tag{A.58}$$

When $f<0$, $4k^2 \le k_x^2+k_y^2$, $k^2 \le (k_x')^2+(k_y')^2$, $k^2 \le (k_x-k_x')^2+(k_y-k_y')^2$

$$\begin{aligned}\mathrm{DI} &= \frac{1}{N_xN_y}\sum_{n_y=0}^{N_y-1}\sum_{n_x=0}^{N_x-1}\hat{P}_{d_0}(n_x,n_y,n_f)\hat{P}_{d_0}(m_x-n_x,m_y-n_y,n_f)\\ &\times\frac{e^{-(z_1-z_0)[k_z'(n_x,n_y)+k_z''(m_x-n_x,m_y-n_y)]}-e^{-(z_1-z_0)k_{z2}(m_x,m_y)}}{k_{z2}^2(m_x,m_y)-\left[k_z'(n_x,n_y)+k_z''(m_x-n_x,m_y-n_y)\right]^2},\\ &(m_x=0,...M_x-1,\quad m_y=0,...M_y-1)\end{aligned} \tag{A.59}$$

When $f > 0$, $4k^2 > k_x^2 + k_y^2$, $k^2 > (k'_x)^2 + (k'_y)^2$, $k^2 > (k_x - k'_x)^2 + (k_y - k'_y)^2$

$$\begin{aligned}
\text{DI} &= \frac{1}{N_x N_y} \sum_{n_y=0}^{N_y-1} \sum_{n_x=0}^{N_x-1} \hat{P}_{d_0}(n_x, n_y, n_f) \hat{P}_{d_0}(m_x - n_x, m_y - n_y, n_f) \\
&\quad \times \frac{e^{-j(z_1-z_0)[k'_z(n_x,n_y)+k''_z(m_x-n_x,m_y-n_y)]} - e^{-j(z_1-z_0)k_{z2}(m_x,m_y)}}{k_{z2}^2(m_x,m_y) - [k'_z(n_x,n_y) + k''_z(m_x-n_x,m_y-n_y)]^2}, \\
&\quad (m_x = 0, ...M_x - 1, \quad m_y = 0, ...M_y - 1)
\end{aligned} \tag{A.60}$$

When $f > 0$, $4k^2 > k_x^2 + k_y^2$, $k^2 > (k'_x)^2 + (k'_y)^2$, $k^2 \leq (k_x - k'_x)^2 + (k_y - k'_y)^2$

$$\begin{aligned}
\text{DI} &= \frac{1}{N_x N_y} \sum_{n_y=0}^{N_y-1} \sum_{n_x=0}^{N_x-1} \hat{P}_{d_0}(n_x, n_y, n_f) \hat{P}_{d_0}(m_x - n_x, m_y - n_y, n_f) \\
&\quad \times \frac{e^{-(z_1-z_0)[jk'_z(n_x,n_y)+k''_z(m_x-n_x,m_y-n_y)]} - e^{-j(z_1-z_0)k_{z2}(m_x,m_y)}}{k_{z2}^2(m_x,m_y) - [k'_z(n_x,n_y) + k''_z(m_x-n_x,m_y-n_y)]^2}, \\
&\quad (m_x = 0, ...M_x - 1, \quad m_y = 0, ...M_y - 1)
\end{aligned} \tag{A.61}$$

When $f > 0$, $4k^2 > k_x^2 + k_y^2$, $k^2 \leq (k'_x)^2 + (k'_y)^2$, $k^2 > (k_x - k'_x)^2 + (k_y - k'_y)^2$

$$\begin{aligned}
\text{DI} &= \frac{1}{N_x N_y} \sum_{n_y=0}^{N_y-1} \sum_{n_x=0}^{N_x-1} \hat{P}_{d_0}(n_x, n_y, n_f) \hat{P}_{d_0}(m_x - n_x, m_y - n_y, n_f) \\
&\quad \times \frac{e^{-(z_1-z_0)[k'_z(n_x,n_y)+jk''_z(m_x-n_x,m_y-n_y)]} - e^{-j(z_1-z_0)k_{z2}(m_x,m_y)}}{k_{z2}^2(m_x,m_y) - [k'_z(n_x,n_y) + k''_z(m_x-n_x,m_y-n_y)]^2}, \\
&\quad (m_x = 0, ...M_x - 1, \quad m_y = 0, ...M_y - 1)
\end{aligned} \tag{A.62}$$

When $f > 0$, $4k^2 > k_x^2 + k_y^2$, $k^2 \leq (k'_x)^2 + (k'_y)^2$, $k^2 \leq (k_x - k'_x)^2 + (k_y - k'_y)^2$

$$\begin{aligned}
\text{DI} &= \frac{1}{N_x N_y} \sum_{n_y=0}^{N_y-1} \sum_{n_x=0}^{N_x-1} \hat{P}_{d_0}(n_x, n_y, n_f) \hat{P}_{d_0}(m_x - n_x, m_y - n_y, n_f) \\
&\quad \times \frac{e^{-(z_1-z_0)[k'_z(n_x,n_y)+k''_z(m_x-n_x,m_y-n_y)]} - e^{-j(z_1-z_0)k_{z2}(m_x,m_y)}}{k_{z2}^2(m_x,m_y) - [k'_z(n_x,n_y) + k''_z(m_x-n_x,m_y-n_y)]^2}, \\
&\quad (m_x = 0, ...M_x - 1, \quad m_y = 0, ...M_y - 1)
\end{aligned} \tag{A.63}$$

When $f > 0$, $4k^2 \leq k_x^2 + k_y^2$, $k^2 > (k_x')^2 + (k_y')^2$, $k^2 > (k_x - k_x')^2 + (k_y - k_y')^2$

$$\begin{aligned}\mathrm{DI} &= \frac{1}{N_x N_y} \sum_{n_y=0}^{N_y-1} \sum_{n_x=0}^{N_x-1} \hat{P}_{d_0}(n_x, n_y, n_f) \hat{P}_{d_0}(m_x - n_x, m_y - n_y, n_f) \\ &\quad \times \frac{e^{-j(z_1-z_0)[k_z'(n_x,n_y)+k_z''(m_x-n_x,m_y-n_y)]} - e^{-(z_1-z_0)k_{z2}(m_x,m_y)}}{k_{z2}^2(m_x,m_y) - \left[k_z'(n_x,n_y) + k_z''(m_x-n_x,m_y-n_y)\right]^2}, \\ &\quad (m_x = 0, ...M_x - 1, \quad m_y = 0, ...M_y - 1) \end{aligned} \tag{A.64}$$

When $f > 0$, $4k^2 \leq k_x^2 + k_y^2$, $k^2 > (k_x')^2 + (k_y')^2$, $k^2 \leq (k_x - k_x')^2 + (k_y - k_y')^2$

$$\begin{aligned}\mathrm{DI} &= \frac{1}{N_x N_y} \sum_{n_y=0}^{N_y-1} \sum_{n_x=0}^{N_x-1} \hat{P}_{d_0}(n_x, n_y, n_f) \hat{P}_{d_0}(m_x - n_x, m_y - n_y, n_f) \\ &\quad \times \frac{e^{-(z_1-z_0)[jk_z'(n_x,n_y)+k_z''(m_x-n_x,m_y-n_y)]} - e^{-(z_1-z_0)k_{z2}(m_x,m_y)}}{k_{z2}^2(m_x,m_y) - \left[k_z'(n_x,n_y) + k_z''(m_x-n_x,m_y-n_y)\right]^2}, \\ &\quad (m_x = 0, ...M_x - 1, \quad m_y = 0, ...M_y - 1) \end{aligned} \tag{A.65}$$

When $f > 0$, $4k^2 \leq k_x^2 + k_y^2$, $k^2 \leq (k_x')^2 + (k_y')^2$, $k^2 > (k_x - k_x')^2 + (k_y - k_y')^2$

$$\begin{aligned}\mathrm{DI} &= \frac{1}{N_x N_y} \sum_{n_y=0}^{N_y-1} \sum_{n_x=0}^{N_x-1} \hat{P}_{d_0}(n_x, n_y, n_f) \hat{P}_{d_0}(m_x - n_x, m_y - n_y, n_f) \\ &\quad \times \frac{e^{-(z_1-z_0)[k_z'(n_x,n_y)+jk_z''(m_x-n_x,m_y-n_y)]} - e^{-(z_1-z_0)k_{z2}(m_x,m_y)}}{k_{z2}^2(m_x,m_y) - \left[k_z'(n_x,n_y) + k_z''(m_x-n_x,m_y-n_y)\right]^2}, \\ &\quad (m_x = 0, ...M_x - 1, \quad m_y = 0, ...M_y - 1) \end{aligned} \tag{A.66}$$

When $f > 0$, $4k^2 \leq k_x^2 + k_y^2$, $k^2 \leq (k_x')^2 + (k_y')^2$, $k^2 \leq (k_x - k_x')^2 + (k_y - k_y')^2$

$$\begin{aligned}\mathrm{DI} &= \frac{1}{N_x N_y} \sum_{n_y=0}^{N_y-1} \sum_{n_x=0}^{N_x-1} \hat{P}_{d_0}(n_x, n_y, n_f) \hat{P}_{d_0}(m_x - n_x, m_y - n_y, n_f) \\ &\quad \times \frac{e^{-(z_1-z_0)[k_z'(n_x,n_y)+k_z''(m_x-n_x,m_y-n_y)]} - e^{-(z_1-z_0)k_{z2}(m_x,m_y)}}{k_{z2}^2(m_x,m_y) - \left[k_z'(n_x,n_y) + k_z''(m_x-n_x,m_y-n_y)\right]^2}, \\ &\quad (m_x = 0, ...M_x - 1, \quad m_y = 0, ...M_y - 1) \end{aligned} \tag{A.67}$$

APPENDIX

B

Figures for Abersim

In this section, the process for getting the isolated fundamental and second harmonic components from the Abersim is demonstrated. The simulated non-linear ultrasound field is plotted as shown in Fig. B.1. This non-linear field contains all harmonic components which are overlapping each other.

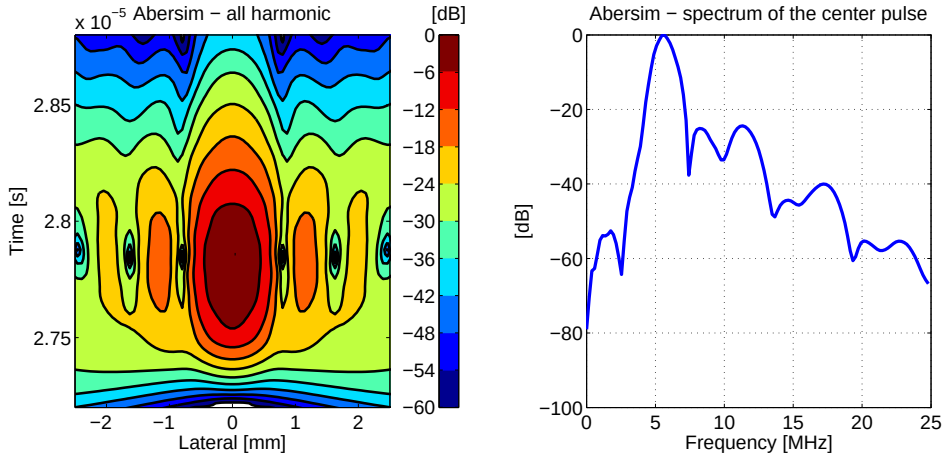

Figure B.1: Abersim simulation results with all harmonic components - This is the raw simulated data by use of Abersim.

Each harmonic component has a certain bandwidth with the border overlapped between two adjacent harmonic components. To separate them, the pulse inversion technique is applied to remove the odd harmonic components by summing or remove the even harmonic components by subtracting the received pulses from two simulations, which are excited by two inverted pulses. Fig. B.2 shows the ultrasound field after removing the even harmonic

components. The spectrum illustrates only the fundamental and third harmonic components are remained after subtractions. The overlapped part between the fundamental and third harmonic components is very small and can be ignored. Thus, a bandpass filter can be used to remove the third one and only the fundamental component is left as shown in Fig. B.3.

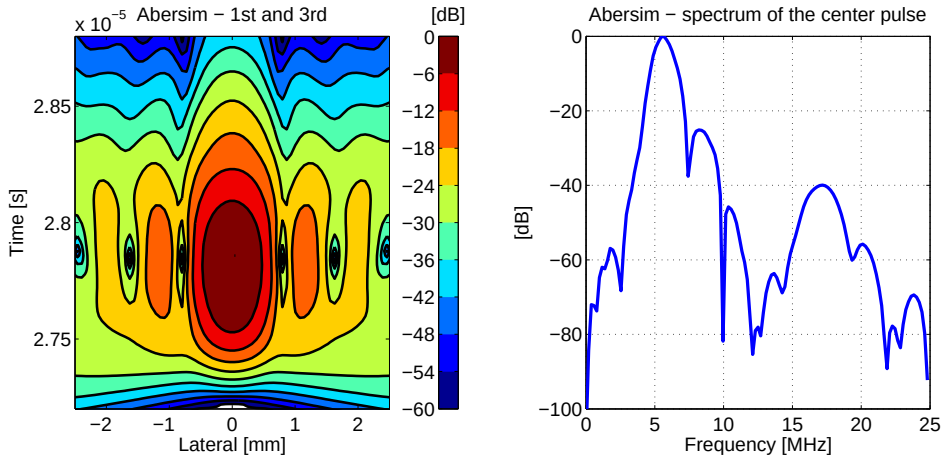

Figure B.2: Abersim simulation results with the fundamental and third harmonic components - This is obtained by subtracting two simulated results.

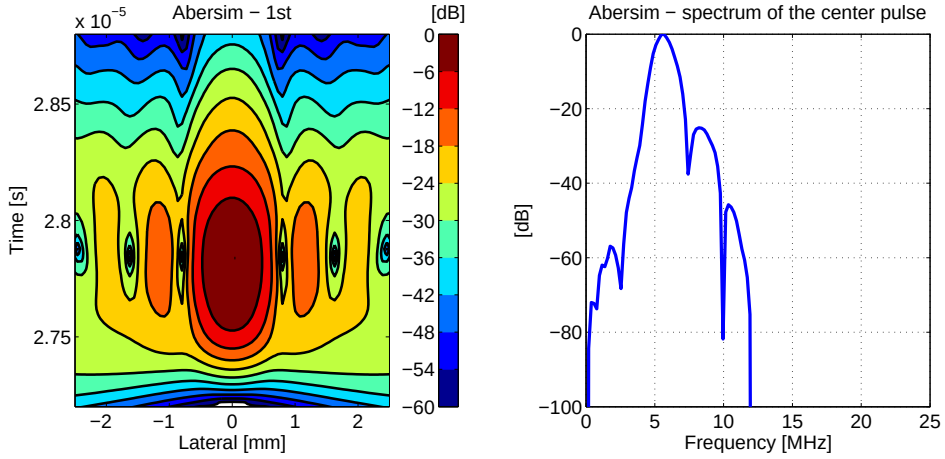

Figure B.3: Abersim simulation results of the fundamental component - This is obtained by applying a bandpass filter to the results shown in Fig. B.2 to isolate the fundamental component.

Likewise, by summing the received pulses the even harmonic components are obtained as shown in Fig. B.4. Similarly, the pure second harmonic component is isolated by filtering out the sub and fourth harmonic components as shown in Fig. B.5.

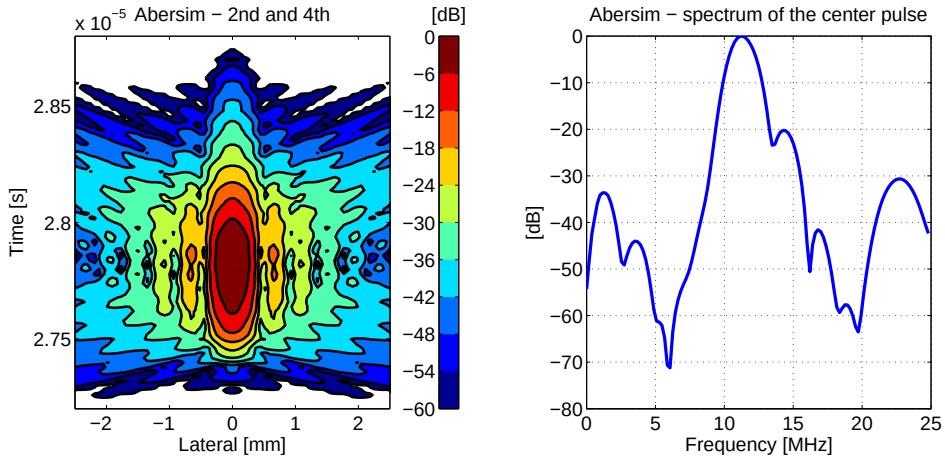

Figure B.4: Abersim simulation results with the second and fourth harmonic components - This is obtained by summing two simulated results.

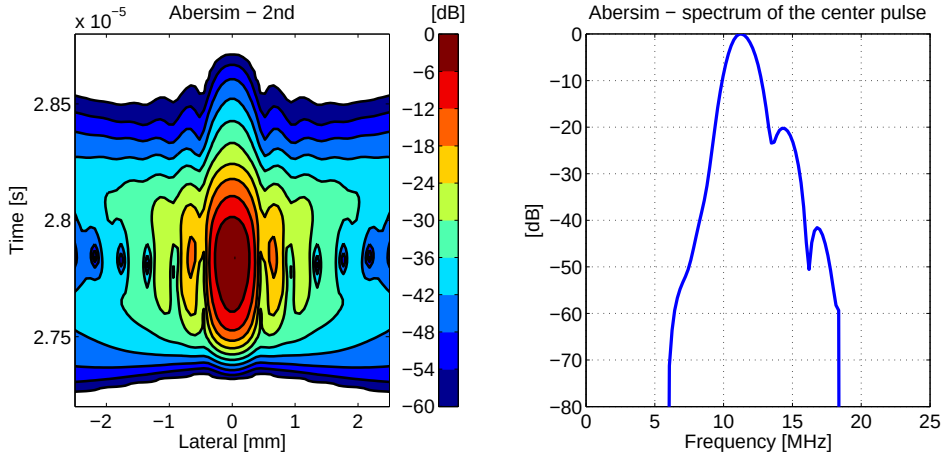

Figure B.5: Abersim simulation results of the second harmonic component - This is obtained by applying a bandpass filter to the results shown in Fig. B.4 to isolate the second harmonic component.

APPENDIX

C

Publications

C.1 Conference paper I - Feasibility of non-linear simulation for Field II using an angular spectrum approach

- Yigang Du and Jørgen Arendt Jensen, "Feasibility of non-linear simulation for Field II using an angular spectrum approach", presented at *IEEE - Ultrasonics Symposium* in Beijing, China, 2008, pp. 1314-1317

C.2 Conference paper II - Angular spectrum simulation of pulsed ultrasound fields

- Yigang Du, Henrik Jensen and Jørgen Arendt Jensen, "Angular spectrum simulation of pulsed ultrasound fields", presented at *IEEE - Ultrasonics Symposium* in Rome, Italy, 2009, pp. 2379-2382

C.3 Journal paper I - Angular spectrum approach for simulating pulsed ultrasound fields

- Yigang Du, Henrik Jensen and Jørgen Arendt Jensen, "Angular spectrum approach for simulating pulsed ultrasound fields", submitted for publishing in *Ultrasonics - Elsevier*, 2011

C.4 Conference paper III - Simulation of second harmonic ultrasound fields

- Yigang Du, Henrik Jensen and Jørgen Arendt Jensen, "Simulation of second harmonic ultrasound fields", presented at *IEEE - Ultrasonics Symposium* in San Diego, California, USA, 2010

C.5 Conference paper IV - Comparison of simulated and measured non-linear ultrasound fields

- Yigang Du, Henrik Jensen and Jørgen Arendt Jensen, "Comparison of simulated and measured non-linear ultrasound fields", presented at *SPIE - Medical Imaging* in Orlando, Florida, USA, 2011, vol. 79680P, pp. 1-10

C.6 Journal paper II - Fast non-linear pulsed ultrasound field simulation using an angular spectrum approach

- Yigang Du, Henrik Jensen and Jørgen Arendt Jensen, "Fast non-linear pulsed ultrasound field simulation using an angular spectrum approach", submitted for publishing in *Journal of the Acoustical Society of America*, 2011

C.7 Conference abstract I - Angular spectrum approach for fast simulation of pulsed non-linear ultrasound fields

- Yigang Du, Henrik Jensen and Jørgen Arendt Jensen, "Angular spectrum approach for fast simulation of pulsed non-linear ultrasound fields", abstract submitted to *IEEE - Ultrasonics Symposium* in Orlando, Florida, USA, 2011

C.8 Conference abstract II - Second harmonic imaging using synthetic aperture sequential beamforming

- Yigang Du, Joachim Rasmussen, Henrik Jensen and Jørgen Arendt Jensen, "Second harmonic imaging using synthetic aperture sequential beamforming", abstract submitted to *IEEE - Ultrasonics Symposium* in Orlando, Florida, USA, 2011